Computational and Experimental Approach for Non-destructive Testing by Laser Shearography

A Thesis

submitted to the faculty of the

Worcester Polytechnic Institute

as a partial fulfillment of the requirements for the

Degree of Master of Science

In

Mechanical Engineering

By

_____

Xiaoran Chen

24 June 2014

Approved:

_____

Prof. Cosme Furlong, Advisor

_____

Prof. John M. Sullivan, Member, Thesis Committee

_____

Prof. Allen H. Hoffman, Member, Thesis Committee

_____

Prof. Pilar Arroyo, University of Zaragoza, Spain, Member, Thesis Committee

_____

Prof. Raghvendra V. Cowlagi, Graduate Committee Representative

Abstract

Non-destructive testing (NDT) is critical to many precision industries because it can provide important information about the structural health of critical components and systems. In addition, NDT can also identify situations that could potentially lead to critical failures. Specifically, NDT by optical methods have become popular because of their non-contact and non-invasive nature. Shearography is a high-resolution optical NDT method for identification and characterization of structural defects in components and has gained wide acceptance over the last decade. Traditional workflow of NDT by shearography has been determined to be inefficient, due to the requirements of having experienced operators that must determine the most suitable loading methods to identify defects in samples under testing as well as to determine the best system arrangement for obtaining the maximum measuring sensitivity.

To reduce the number of experiments that are required and to allow inspectors to perform NDT by laser shearography in a more efficient way, it is necessary to optimize the experimental workflow. The goal of the optimization would be an appropriate selection of all experimental variables including loading methods, boundary conditions, and system's sensitivities, in order to avoid repeating experiments several times in the processes of components characterization and health monitoring.

To achieve this goal, a hybrid approach using shearographic fringe prediction with Finite Element Analysis (FEA) has been developed. In the FEA simulations, different loading conditions are applied to samples with defects, and in turn, the shearographic fringes are predicted. Fringe patterns corresponding to specific loading conditions that

are capable of detecting defects are chosen and experimental tests are performed using those loading conditions. As a result, using this approach, inspectors could try different combinations of loading methods, and system's sensitivities to investigate and select appropriate experimental parameters to improve defect detection capabilities of the system by using low-cost computer simulations instead of lengthy and expensive experiments.

In addition, to improve the identification of defects on the sample, camera calibration and image registration algorithms are used to project the detected defects on the sample itself to locate and visualize the position of defects during shearographic investigations.

This hybrid approach is illustrated by performing NDT of a plate made of acrylic that has a partial hole at the center. Fringe prediction with finite element analysis are used to characterize the optimized experimental procedures and in turn, corresponding measurements are performed. A multimedia projector is employed to project the defects on the surface of the plate in order to visualize the location of the partial hole (defect). Furthermore, shearographic system is used for other applications including NDT of a composites plate and of a thin latex membrane. The procedures shows the effectiveness of the approach to perform NDT with shearography methods.

The thesis is dedicated proudly to my family

Acknowledgements

Table of Contents

List of figures

Nomenclature

CCD	Charged Coupled Device
DSS	Digital Sheaography System
FEA	Finite Element Analysis
FFT	Fast Fourier Transform
IPT	Image Processing Toolbox
NDT	Non-destructive testing
PZT	piezoelectric transducer
SLM	Spatial Light Modulator
TM	Tympanic membrane (Eardrum)
$I_A(x, y)$	Speckle pattern intensity stored by CCD camera
$\psi(x, y)$	Randomly distributed phase difference between the original image and sheared image
$\boldsymbol{L}(x, y)$	Displacement field vector
$\boldsymbol{K}(x, y)$	Sensitivity vector - the bisector between the observation vector and the illumination vector.

S	Strain tensor
Ω	Optical phase
λ	Optical wavelength
θ	The angle between the illumination direction and the average local surface normal of the object
W	Normal surface displacement
h	Thickness of the plate
E	Young's Modulus
μ	Passion's ratio
σ_{rr}	Radial stress
$\sigma_{\theta\theta}$	Circumferential stress
$\sigma_{r\theta}$	Tangential stress
T	Transformation function

Objectives

This project is focused on the development of procedures to perform non-destructive testing (NDT) with laser shearography.   The objective is to develop a hybrid approach that includes applying sheraographic fringe prediction and Finite Element Analysis (FEA) to obtain optimized laser shearography NDT procedures to improve the efficiency of characterization and health monitoring of components.   Also, camera calibration and image registration algorithms are used in the development of methods to project shearography data onto the components under test in order to locate and visualize the position of defects in real-time.

1. Introduction

1.1 Non-destructive testing (NDT)

Non-destructive testing (NDT) refers to a large group of techniques that are used in various industries and engineering fields to monitor the health of a material, component, or system in a structure without causing damage [Bajoria, 2009]. The main goal of NDT is to ensure that structural components and systems perform their function in a reliable way. NDT can detect potential failures in critical components and systems as well as inform users of the appropriate time to replace their components accounting to safety and performance. As a result, NDT has become a highly valuable and critical technique in many precision industries, as it can save both money and time in product evaluation, troubleshooting, and research.

The field of NDT is broad and there are many methods for performing NDT [Prakash et al., 2009]. These methods of testing vary within different applications; for example, strain gages have traditionally been used to find locations with high stress concentration, which indicates some potential failure of components. However, due to the newer advanced requirements for high accuracy and low processing times, many new NDT techniques have flooded market in recent years, as is shown in Figure 1.1.
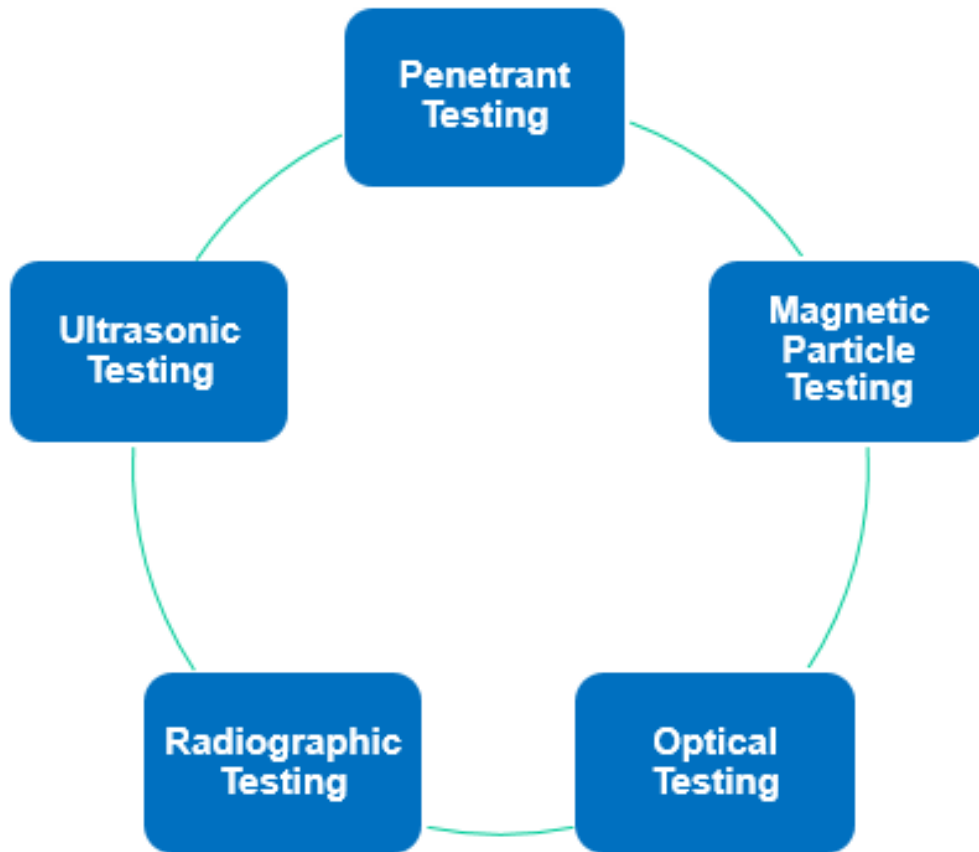
Figure 1.1.   Different NDT techniques exist in various industries

Magnetic particle NDT testing uses a magnetic field to test a ferromagnetic material and then dusts the surface using iron particles.   By analyzing the iron particles which can form visible patterns because of distorted magnetic fields, defects can be detected.

In radiographic NDT, which is a technique that uses x-ray or gamma ray radiation, defects are detected by differences in radiation absorption in the material.   These differences are visible on a shadow graph displayed on photographic film or a fluorescent

screen.

Ultrasonic testing uses high frequency sound waves to examine the sample under testing. By analyzing the irregular amount of energy received by the detector, defects can be located. However, it may be difficult to inspect thin parts by ultrasonic means because the amount of energy change is too small to distinguish.

The above techniques, although helpful, are only suitable for limited applications due to issues of highly required environmental and experimental conditions.   For some NDT techniques, regulations require samples under testing to be cleaned, otherwise, the testing may result in false indications, thereby causing confusion.   Additionally, for some NDT techniques, while it is easier to obtain a test signal from their detector, it is difficult to interpret the results correctly.   However, optical laser testing is a potential solution, as it uses laser light to illuminate samples under testing.   With this method, when light is reflected from a sample of interest, any flow modifies the light intensity.   Therefore, flows are indicated by irregularities in changes to light intensity.   This method is especially suitable because it is non-invasive and its results are easier for engineers to interpret [Engineeringtoolbox website].

1.2 Laser shearography

Speckle shearing interferometry, also called shearography, is a full field non-contact

optical metrology technique typically used to measure the first derivative of the surface

displacement that is exacted by mechanical or thermal load [Francis et al., 2010].

Shearography is a high-resolution optical NDT method that has become increasingly

popular, not only due to its ability to provide non-contact, full field measurements, but also

its resiliency to environmental disturbances.   In other words, the shearography system is

portable and allows us to go outside of the optics lab to perform tests in real environments,

even in those that are harsh.   Because of these positive features, shearography can be used

in many different applications.   One of the main application of shearography is the

inspection of the quality of composites and other materials, which are used in aerospace,

automobile, art conservation, and wind energy industries.   Other representative

applications are shown in Figure 1.2.

Art Conservation   Aerospace   Civil Engineering   Transporation
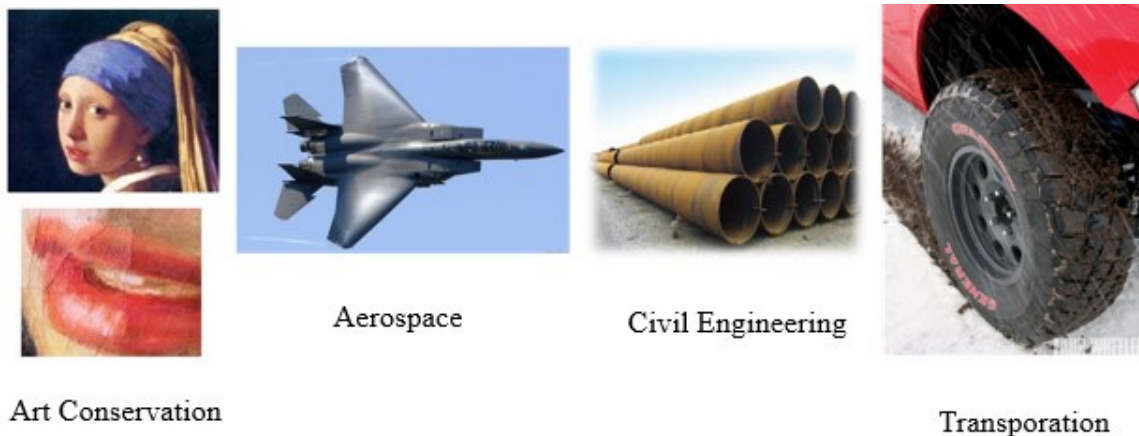
Figure 1.2.   Application of Laser shearography (NDT) in various industries
[Francis et al., 2010; Zervas 2011; Khaleghi et al., 2012]

1.3 Finite element analysis and laser shearography

One of the improvements that can be made to NDT by shearography is the addition of finite element analysis (FEA).   The main goal of introducing FEA to laser shearography is to utilize FEA's unique and advantageous ability to simulate deformations, which are induced through different excitation loads on samples under tested.   In practice, many samples under testing have complex geometries.   FEA allows the sample of interest to be divided into multiple small regions, termed "finite elements."   Each region's physical behavior can be mathematically calculated in a concise manner and then combined into a large matrix equation.   This equation can then be solved to determine the existence of a deformation that results from a loading condition.   As a result, if inspectors use FEA before conducting NDT with laser shearography, they would have better knowledge of how to apply the excitation load to the sample by viewing the simulated deformation results of the sample.   Thus, the inspector would have a clearer idea of how to introduce the desired deformation in real testing.   Therefore, FEA allows us to bypass the disadvantage of needing to try different excitation methods to find defects, ultimately allowing inspectors to perform NDT more effectively [Kreis, 2005; Joshi, 2010].

1.4 Developed shearography inspection workflow scheme

A typical workflow of NDT by laser shearography is shown in Figure 1.3 [Hung, 1982;

Kreis, 2005; Francis et al., 2010].
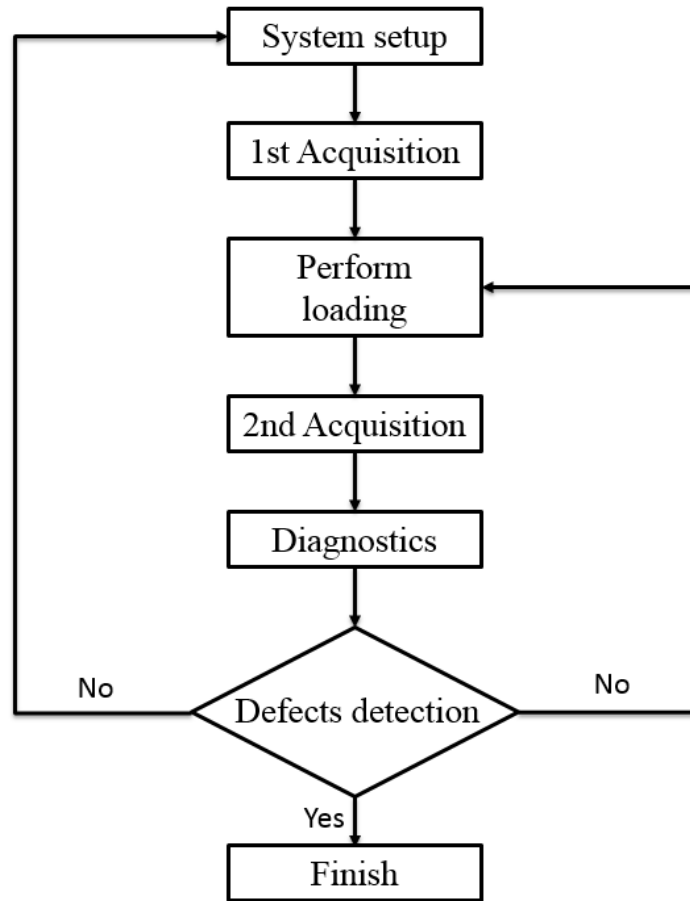
Figure 1.3.   Typical NDT workflow by laser shearography

The workflow shown in Figure 1.3, includes seven steps and uses a top-to-bottom strategy.   This strategy, however, has been determined to be largely inefficient, as it requires a great deal of effort by experienced operators who must determine the most

6

suitable loading methods for identifying defects in samples under testing, as well as determining the best system arrangement for obtaining the highest image quality [Osten et al., 2010].

This thesis is focused on the development of a NDT workflow by using laser shearography system.   The objective is to develop a hybrid approach which applies fringe predict technique with Finite Element Analysis (FEA) to do NDT testing by laser shearography to assist and speed up defect detection.   Also, camera calibration and image registration algorithms are used to project the detected defect on the sample itself to locate and visualize the position of defects during shearographic investigations to facilitate engineers work.   The updated workflow is shown in Figure 1.4.
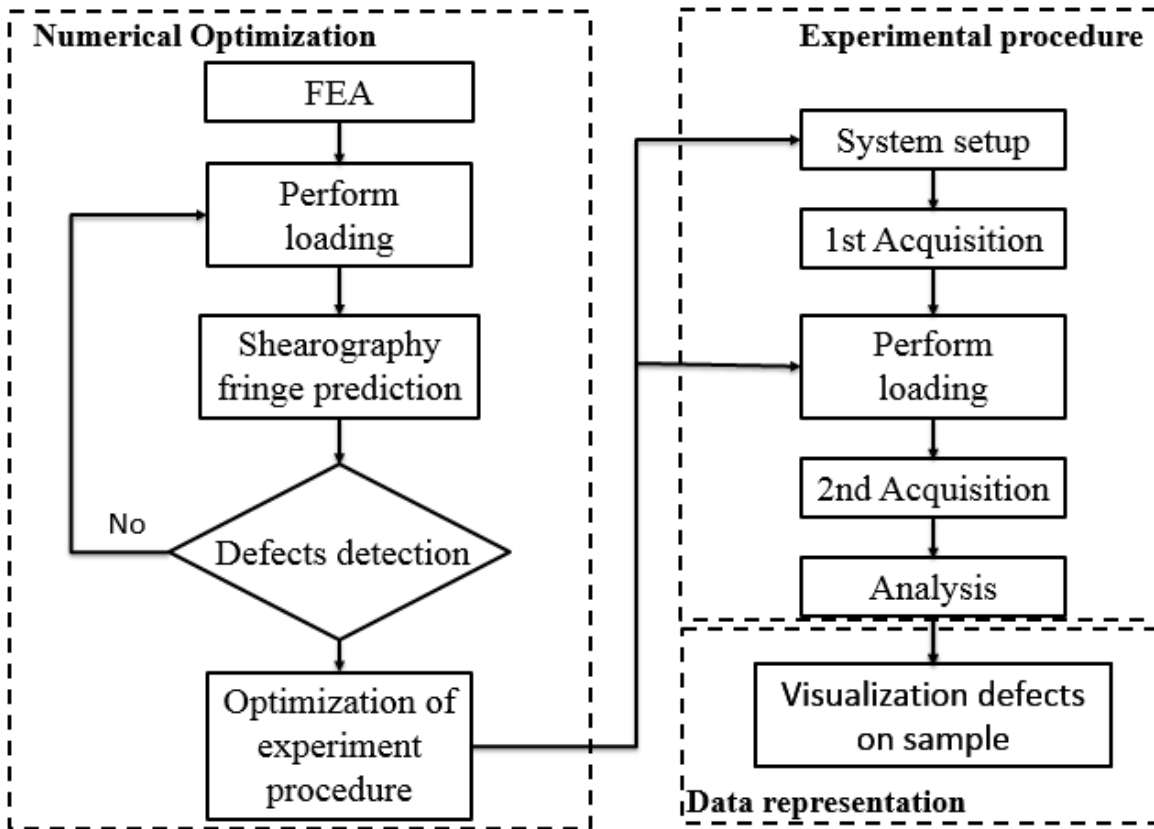
Figure 1.4.   Combination of the typical top-to-bottom shearography NDT strategy with shearography fringe simulations by FEA, as developing in this Thesis

By introducing FEA into the workflow, the inspector is able to have a better idea of how to introduce the desired deformation to the sample under test.   In addition, FEA aids in the planning phase of laser shearography measurements to allow the design of an enhanced experimental setup and arrangement [Kreis, 2005].   With an improved setup, it is possible to determine whether an expected loading method produces sufficiently high, yet not too high, density fringes, based on simulations—requiring much lower effort and reduced costs than conventional methods.

In the last step of updated workflow, Figure 1.4, a multimedia projector is also introduced, allowing the shearography results to be projected back onto the surface of the real sample.   Adding this step makes the process of locating and then marking defects on the real samples easier for engineers.   Thus, shearography can be used as a relatively fast tool for locating and marking defects, even by engineers who have limited experience with shearography.

2. Laser shearography

2.1 Laser shearography system overview

Electronic shearography is an interferometric technique that permits full-field observation of surface displacement gradients. In 1982, Hung presented a schematic diagram of shearography, shown in Figure 2.1, using a thin glass wedge located in the iris plane of the lens that covers one-half of the lens aperture [Hung, 1982; Francis et al., 2010; Khaleghi et al., 2012].
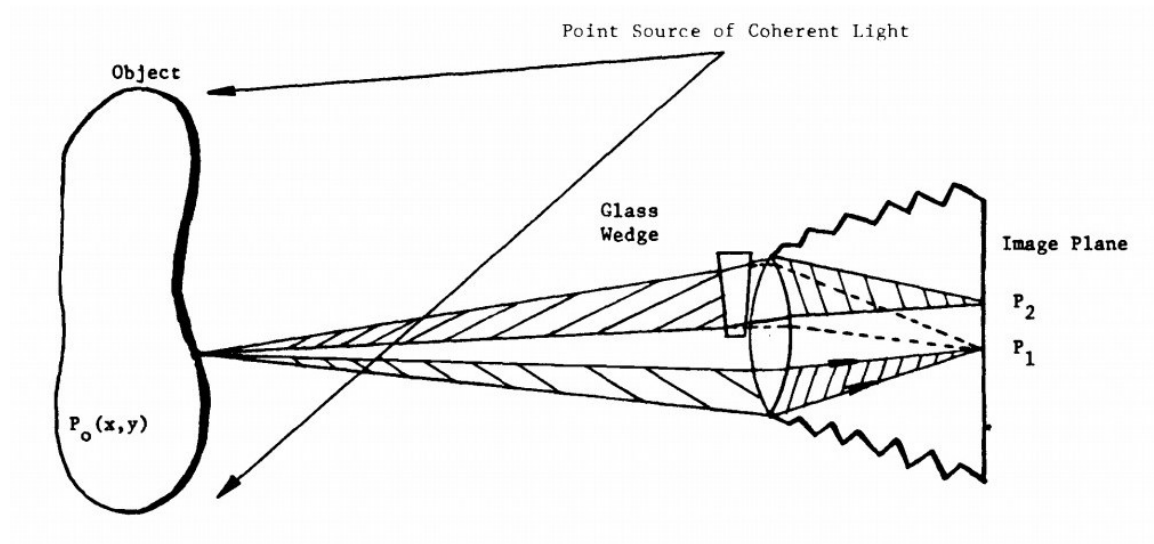
Figure 2.1.   Schematic diagram of shearography [Hung, 1982]

The glass wedge, which is a small angle prism, diverges rays passing through it.   As a

result, two laterally sheared images are captured by the image plane, and the two sheared images interfere to produce a speckle pattern.   When the sample is deformed, the pattern is slightly changed.   By subtracting the deformed patterns from the un-deformed patterns, we can obtain a shearography pattern that is rated to the surface displacement gradient of the sample [Hung, 1982].

In recent years, many improvements have been made in electronic shearography, including the Michelson configuration, which is gaining wide acceptance.   The principle of a digital shearography system using the Michelson configuration is illustrated in Figure 2.2 [Khaleghi et al., 2012].   In the Michelson method, two mirrors are placed perpendicular to each other, and therefore, the combined beams coming into the CCD sensor after the beam splitter are collinear.

In a shearography system, as shown in Figure 2.2, the mirror facing the CCD can be rotated—this mirror is called a shearing mirror.   In some cases, a piezoelectric transducer (PZT) is mounted on the reference mirror such that the system can perform phase-stepping shearography.   As the shearing mirror is rotated, two identical but displaced images are recorded by the CCD camera. The two images combine coherently to produce an interferometric speckle pattern captured by the CCD sensor [Pryputniewicz, 1992; Falldorf et al., 2003; Kreis, 2005].

In order to introduce a constant phase shift in the modified Michelson arrangement, the

PZT is displaced by a set amount of sub-micrometers displacements.   Thus, the accurate

calibration of the voltage to the PZT is necessary for an accurate phase step.
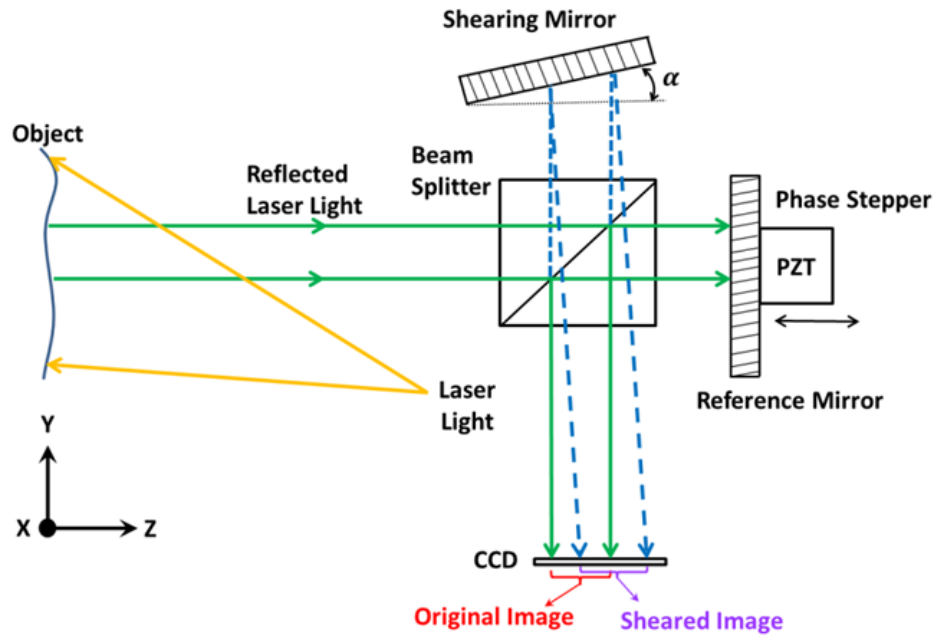
Figure 2.2.   Schematic of the optical configuration of the shearography system using
Michelson configuration currently under development [Khaleghi et al., 2012]

BIAS developed a new shearing interferometer which is based on a reflective liquid

crystal Spatial Light Modulator (SLM), is shown in Figure 2.3 [Kalms et al., 2003; Falldorf

et al., 2009].   A diffraction grating with an SLM that has a blazed structure is used to shift

incoming light linearly.   In this process, the fast axis's refractive index can be shifted by

electronically changing the corresponding pixel's value.   The slow axis does not change,

and consequently, the result is two images of an object superimposed onto the CCD chip.

12
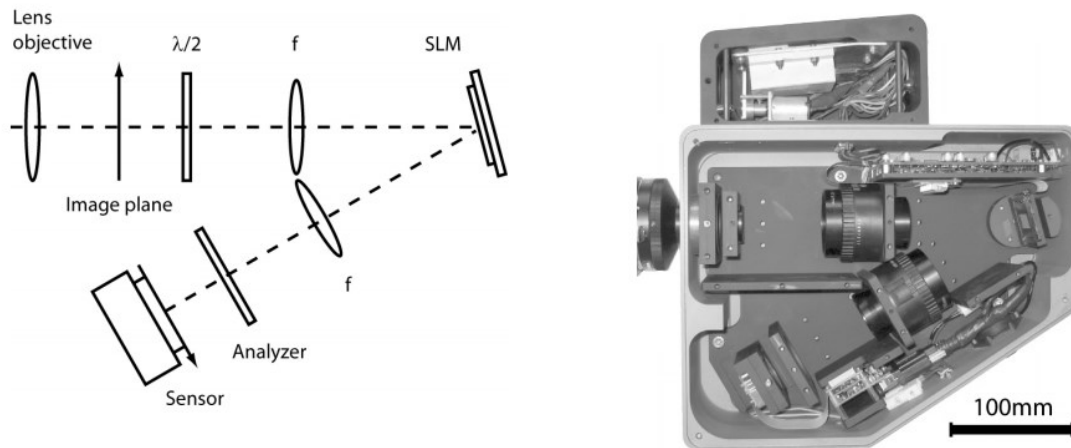
Figure 2.3.   Scheme of a compact shearing interferometer that makes use of the birefringent properties of a liquid crystal spatial phase modulator [Falldorf et al., 2009]

Because it is possible to control the duration and the orientation of the blaze grating, the magnitude and direction of shear can be adjusted.   Thus, this configuration is flexible while also being highly reproducible, and in addition, the phase shifting algorithm can be applied with the use of the SLM, eliminating the need to use parts that move mechanically.

In our work, we use the Michelson configuration because of the simplistic design, the adjustment capabilities of the image shear, and the fact that phase analysis through the temporal phase stepping technique can be easily implemented by mounting one of the mirrors on a piezo-electric transducer (PZT) [Francis et al., 2010; Khaleghi et al., 2012]. Figure 2.4 shows a packaged version of the shearography system based on Michelson configuration.
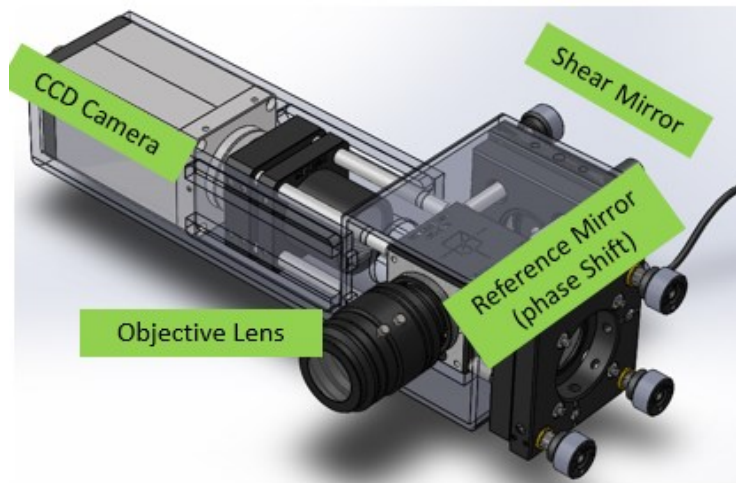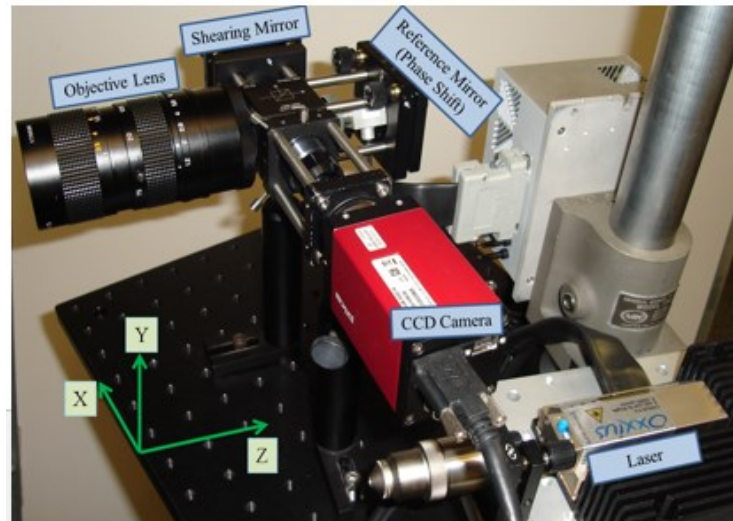
Figure 2.4.   Shearography system based on a Michelson configuration: (a) CAD model of the opto-mechanical design; and (b) realized system [Chen et al., 2014]

2.2 Principles of laser shearography

In a shearography system, two slightly spatially shifted speckle fields of the rough surface are superposed.   The shifting of the speckle fields is performed by a shearing

element, e.g. a glass wedge in front of one half of the imaging lens, two tilted glass plates, or a Michelson interferometer-like arrangement with one mirror slightly tilted.

Let the two wave fields be separated laterally by the mutual shearing Δx, and then we obtain two nearly collinear wave fields [Kreis, 2005],

$$E_1(x,y) = E_{01}(x,y)e^{i\emptyset(x,y)}, \tag{1}$$

$$E_2(x,y) = E_{02}(x,y)e^{i\emptyset(x+\Delta x,,y)}.$$

Their interference produces the speckle pattern,

$$I_A(x,y) = |E_1(x,y) + E_2(x,y)|^2 =$$

$$I_1(x,y) + I_2(x,y) + 2\sqrt{I_1(x,y)I_2(x,y)}cos\psi(x,y), \tag{2}$$

which is recorded, digitized, and stored by a CCD camera. $\psi(x,y)$ is the randomly distributed phase difference between the original image and sheared image, $\psi(x,y) = \phi(x,y) - \phi(x+\Delta x,y)$. Deformation of the object leads to the wave fields,

$$E_3(x,y) = E_{01}(x,y)e^{i[\emptyset(x,y)+\Delta\emptyset(x,y)]},$$

$$E_4(x,y) = E_{02}(x,y)e^{i[\emptyset(x+\Delta x,,y)+\Delta\emptyset(x+\Delta x,,y)]}, \tag{3}$$

whose superposition yields the speckle pattern

$$I_B(x,y) = I_1(x,y) + I_2(x,y) +$$

$$2\sqrt{I_1(x,y)I_2(x,y)}cos[\psi(x,y) + \Delta\emptyset(x,y) - \Delta\emptyset(x+\Delta x,y)], \tag{4}$$

15

and with the use of Equations 2 and 4, it is possible to obtain

$$\frac{\Delta\emptyset(x,y)-\Delta\emptyset(x+\Delta x,y)}{2} = \frac{\delta L(x,y)}{\delta x} \cdot \frac{\pi\Delta x}{\lambda} K(x,y) \ , \tag{5}$$

where $L(x,y)$ is the displacement field vector, $\frac{\delta L(x,y)}{\delta x}$ is the gradient of $L(x,y)$ along the shearing direction, λ is the wavelength of the laser used, and $K(x,y)$ is the sensitivity vector. The sensitivity vector is defined to be the bisector between the observation and illumination vectors as follows,

$$K(x,y) = K_2 - K_1 \ , \tag{6}$$

where K_1 is the illumination vector and K_2 is the observation vector. Therefore, the optical phase difference, Equation 5, can be written as [Pryputniewicz, 1993; Kreis, 2005],

$$\Omega = \frac{2\pi}{\lambda}(k_x\frac{\delta L_x}{\delta x} + k_y\frac{\delta L_y}{\delta x} + k_z\frac{\delta L_z}{\delta x})\Delta x \ , \tag{7}$$

where Ω is the optical phase difference of an object under investigation before and after deformations, $\frac{\delta L_x}{\delta x}$, $\frac{\delta L_y}{\delta x}$, and $\frac{\delta L_z}{\delta x}$ are the gradients of the displacement vector, $L = (L_x, L_y\ L_z)$ along the shearing direction, and Δx is the magnitude of the applied shear, respectively. k_x, k_y, and k_z are the components of the sensitivity vector, which is defined by the geometry of the shearography system.

Based on Equation 7, the sensitivity vector is able to define the system sensitivity, which controls the quality of the phase fringes that are produced by a specific loading conditions of the sample under investigation. Shearography is sensitive to both, displacement

gradients that are determined by the sensitivity vector as well as the direction and magnitude

of the applied shear.   For example, if the displacement vector of the sample under test is in

the out-of-plane direction, but the sensitivity vector is in a horizontal or vertical direction,

the system is not able to produce shearography fringes.   In this case, even if the sample has

defects, inspectors will not be able to detect them in such shearography arrangement [Kreis,

2005; Francis et al., 2010; Khaleghi et al., 2012].

By defining the observation and illumination directions to be approximately collinear,

the k_x, k_y components of the sensitivity vector are approximately zero,   so that the

system is predominantly sensitive to the out-of-plane displacement gradient to yield,

$$\Omega = \frac{4\pi}{\lambda \cos\theta} \frac{\delta L_z}{\delta s} \Delta s \ ,$$

(8)

where θ is the angle between the illumination direction and the average local surface

normal of the object and $\Delta s = \Delta x$ or $\Delta s = \Delta y$, depending on applied shearing direction.

Near parallel illumination-observation makes the conditions $\cos\theta \approx 1$, and thus, two of the

out-of-plane displacement derivatives can be computed with,

$$\frac{\delta L_z}{\delta x} = \frac{\lambda \Omega}{4\pi \Delta x} \quad \text{and} \quad \frac{\delta L_z}{\delta y} = \frac{\lambda \Omega}{4\pi \Delta y} \ ,$$

(9)

which indicates that the out-of-plane displacement gradient is proportional to the optical

phase change before and after deformations.

A strain tensor, S, is defined by nine components, including three normal and six shear

components,

$$S = \begin{bmatrix} \frac{\delta L_x}{\delta x} & \frac{1}{2}(\frac{\delta L_x}{\delta y} + \frac{\delta L_y}{\delta x}) & \frac{1}{2}(\frac{\delta L_x}{\delta z} + \frac{\delta L_z}{\delta x}) \\ \frac{1}{2}(\frac{\delta L_x}{\delta y} + \frac{\delta L_y}{\delta x}) & \frac{\delta L_y}{\delta y} & \frac{1}{2}(\frac{\delta L_y}{\delta z} + \frac{\delta L_z}{\delta y}) \\ \frac{1}{2}(\frac{\delta L_x}{\delta z} + \frac{\delta L_z}{\delta x}) & \frac{1}{2}(\frac{\delta L_y}{\delta z} + \frac{\delta L_z}{\delta y}) & \frac{\delta L_z}{\delta z} \end{bmatrix} . \tag{10}$$

According to Equation 9 and near parallel illumination-observation conditions, only two strain components of tensor S can be determined. In order to measure the additional strain components in Equation 10, namely $\frac{\delta L_x}{\delta x}$, $\frac{\delta L_x}{\delta y}$, $\frac{\delta L_y}{\delta x}$, $\frac{\delta L_y}{\delta y}$, $\frac{\delta L_z}{\delta x}$, $\frac{\delta L_z}{\delta y}$, methods based on multiple directions of illumination or observation can be applied [Groves et al., 2007; Francis et al., 2010; Khaleghi et al., 2012]. The full definition of the strain tensor requires additional measurements of $\frac{\delta L_x}{\delta z}$, $\frac{\delta L_y}{\delta z}$, and $\frac{\delta L_z}{\delta z}$. However, the measurements of these additional strain components would require measurements into the volume of the object, which would need an optical setup different from a typical shearography arrangement [Groves et al., 2007; Francis et al., 2010].

In practice, however, only two of the first derivatives of the out-of-plane displacement vector are measured, $\frac{\delta L_z}{\delta x}$ and $\frac{\delta L_z}{\delta y}$.

2.3 Shear estimation by FFT algorithm

The amount of optical shear greatly affects the shearography system's sensitivity. An FFT-based algorithm based on the shift theorem of the Fourier Transform is used to

determine the amount of shear [Khaleghi et al., 2014]. When the original image's FFT, $a(x, y)$, is defined by $A(\xi, \eta)$, and based on the shift theorem, the FFT of the sheared image, $b(x, y) = a(x - \Delta x, y - \Delta y)$, is calculated with

$$B(\xi, \eta) = e^{-i2\pi(\xi \Delta x + \eta \Delta y)} A(\xi, \eta), \tag{11}$$

and the FFT of the superposed image, $c(x, y) = a(x, y) + a(x - \Delta x, y - \Delta y)$, is

$$C(\xi, \eta) = \left[1 + e^{-i2\pi(\xi \Delta x + \eta \Delta y)}\right] A(\xi, \eta). \tag{12}$$

Magnitudes of shear along horizontal and vertical directions can be calculated approximately by Equations 13 and 14, respectively,

$$\Delta x \approx p_x m_0, \tag{13}$$

$$\Delta y \approx p_y n_0, \tag{14}$$

where p_x and p_y are the width and height of the pixels in the CCD detector, respectively, and m_0 and n_0 are the equivalent amount of shear, specified in number of pixels. Because in our measurements, the width and height of the pixels are equal, then $p_x = p_y$. By discretizing the obtained spectra in the frequency domain, Equation 12 can be rewritten as

$$C(k, l) = \left[1 + e^{-i2\pi\left(k\frac{m_0}{M} + l\frac{n_0}{N}\right)}\right] A(k, l) , \tag{15}$$

where M and N represent the spatial resolution of the entire CCD sensor, $\xi = \frac{k}{Mp_x}$ and $\eta = \frac{l}{Np_y}$ the discretized units in the frequency domain, and k and l are the corresponding

discrete variables. The spatial frequency of the spectrogram of Equation 15 is

$$f_x = \frac{m_0}{M} \ .$$ (16)

Therefore, by combining Equations 13 and 16, the amount of shear is determined by

$$\Delta x \approx p_x \frac{M}{T_x} \ ,$$ (17)

where $T_x = \frac{1}{f_x}$. The same procedures are applied to determine the shear amount along the y-axis. A custom algorithm that can determine the period of the spectrogram's modulated pattern is used to obtain T_x and T_x, as shown in Figure 2.5 [Khaleghi et al., 2014].
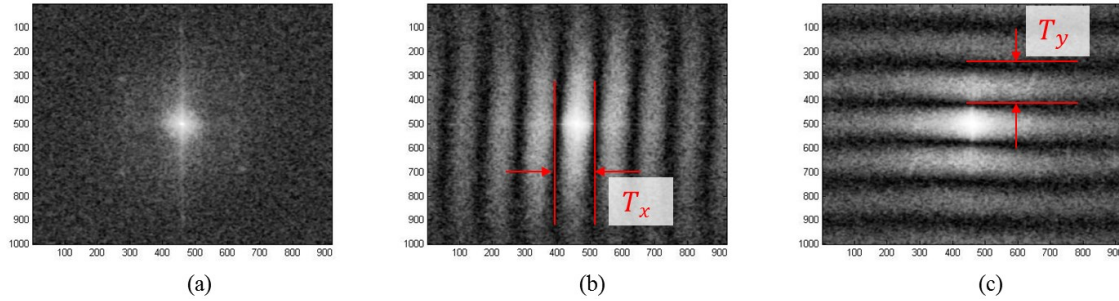
Figure 2.5. Application of FFT algorithms to determine the amount of applied shear: (a) FFT power spectrum of a shearogram without shear; (b) FFT power spectrum of (a) with shear applied in horizontal direction; and (c) FFT power spectrum of (a) with shear applied in the vertical direction [Khaleghi et al., 2014]

2.4 Phase retrieval in laser shearography

As noted in the Section 2.2, the out-of-plane displacement gradient is related to the optical phase. To obtain the first derivative of displacement, optical phase data is extracted

from the images captured using the CCD camera, which allows us to obtain the light intensity of every pixel. The phase map $\Delta\phi(x,y)$ is encoded in the intensity information. Several methods are available for the retrieval of the phase and popular methods include fringe skeletonization [Osten et al., 1993], phase sampling [Creath, 1985], and Fourier transform based methods [Takeda et al., 1982; Ge et al., 2001].

In our setup, we use four-step phase shifting methods: the first phase starting from 0 to 90, 180, and 270 degrees [Pryputniewicz, 1993]. In this method, intensity variations of inteferograms described with Equation 4 and phase shifted by $\frac{\pi}{2}$ are

$$I_1 = I_a + I_b + 2\sqrt{I_a I_b}\,cos(\Omega + 0)\ , \tag{18}$$

$$I_2 = I_a + I_b + 2\sqrt{I_a I_b}\,cos(\Omega + \frac{\pi}{2})\ , \tag{19}$$

$$I_3 = I_a + I_b + 2\sqrt{I_a I_b}\,cos(\Omega + \pi)\ , \tag{20}$$

$$I_4 = I_a + I_b + 2\sqrt{I_a I_b}\,cos(\Omega + \frac{3\pi}{2})\ . \tag{21}$$

Image acquisition must be synchronized with the phase shifter in order for one image to be recorded by the camera at each of the four phase steps. Therefore, our shearography setup synchronizes phase shifting with camera's acquisition. This is achieved by the use of a DAQ system that drives the phase shifter and the camera shutter signal, as shown in Figure 2.6.
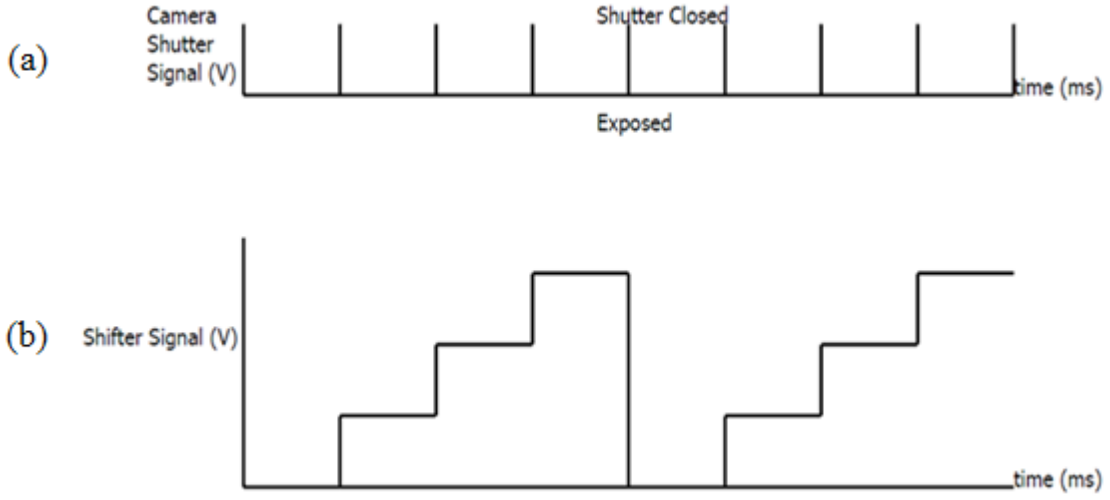
Figure 2.6.   Synchronization in time between (a) camera shutter signal and (b) piezo-electric positioner signal [Tripp, 2012]

To extract optical phase, Ω, that relates to the deformations of an object between exposures, Equations 18 to 21 are written as

$$I_2 = I_a + I_b + 2\sqrt{I_a I_b}\cos(\Omega) \ , \tag{22}$$

$$I_2 = I_a + I_b - 2\sqrt{I_a I_b}\sin(\Omega) \ , \tag{23}$$

$$I_3 = I_a + I_b - 2\sqrt{I_a I_b}\cos(\Omega) \ , \tag{24}$$

$$I_4 = I_a + I_b + 2\sqrt{I_a I_b}\sin(\Omega) \ . \tag{25}$$

By subtracting Equations 25 from 23 as well as Equations 24 from 22, it is obtained that

$$I_4 - I_2 = 4\sqrt{I_a I_b}\sin(\Omega), \tag{26}$$

$$I_1 - I_3 = 4\sqrt{I_a I_b}\cos(\Omega), \tag{27}$$

22

so by dividing Equations 26 and 27,

$$\frac{I_4 - I_2}{I_1 - I_3} = \frac{4\sqrt{I_a I_b}\,\sin(\Omega)}{4\sqrt{I_a I_b}\,\cos(\Omega)} = \tan(\Omega), \tag{28}$$

which renders the solution for Ω modulus 2π, or wrapped phase,

$$\Omega = \tan^{-1}\frac{I_4 - I_2}{I_1 - I_3} \ . \tag{29}$$

Based on Equation 29, we can obtain the phase differences between the original image and the sheared image, which is a reference state phase difference map. Because shearography can measure the gradient of displacement, the object under investigation needs to be deformed. Once the object has deformed, another phase differences map can be obtained. It is called the deformed state phase difference map and computed with

$$\Omega' = \tan^{-1}\frac{I_4' - I_2'}{I_1' - I_3'} \ . \tag{30}$$

As a result, the phase difference of the object before and after deformations can be calculated with Equations 29 and 30

$$\Delta\Omega = \Omega' - \Omega = \tan^{-1}\left[-\frac{(I_1 - I_3)(I_2' - I_4') - (I_2 - I_4)(I_1' - I_3')}{(I_1 - I_3)(I_2' - I_4') + (I_2 - I_4)(I_1' - I_3')}\right]. \tag{31}$$

Figure 2.7. shows the workflow of calculating phase difference map based on four phase stepping algorithm.
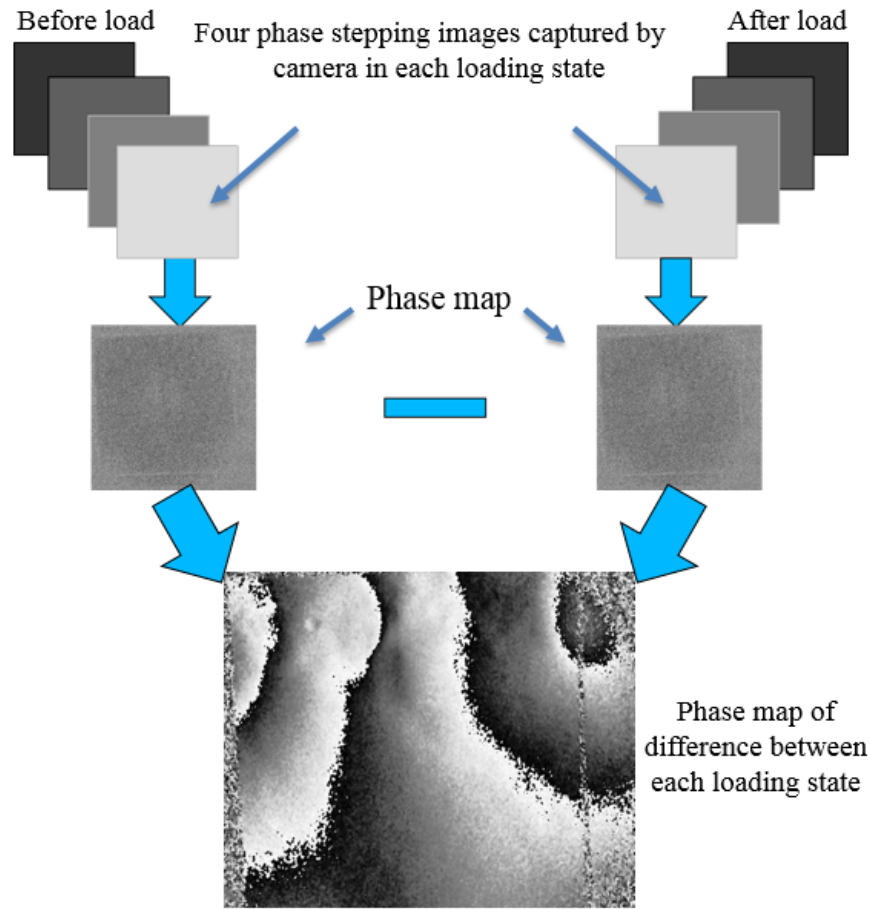
Figure 2.7.   Flowchart describing the general procedure to compute the optical phase difference that corresponds to deformation gradients produced by an applied load to a sample

The phase difference map subtracted between each loading state is limited from $-\pi$ to π because of the nature of the inverse tangent function.   Two consecutive points in $I(x, y)$ can have a sharp discontinuity in height, which is known as phase wrapping. The development of a phase unwrapping algorithm to remove these discontinuities is a major field of research in interferometry [Ghiglia and Pritt, 1998].   In our system the optical phase is unwrapped by spatial and temporal domain algorithms [Harrington et al., 2010;

Zervas, 2011].   The unwrapping algorithms have been optimized and designed specifically

for shearography applications [Furlong et al., 2012; Khaleghi et al., 2012, 2014].

3. Optimization of experimental procedure by finite element analysis and shearography fringe prediction

As noted in Chapter 1, the traditional experimental procedure of NDT by using laser shearography has been determined to be largely inefficient, due to requirements of highly experienced operators who must determine the most suitable loading methods for identifying defects in samples under testing, as well as determining the best system arrangement for obtaining the maximum sensitivity.   As a result, optimization of experimental procedure is needed for reducing the number of experiments required and for reducing experimental costs.   The success of a NDT procedure by using laser shearography is dependent on a number of variables such as loading methods, boundary conditions, sensitivity vectors, the shear direction and the mount of shear.   A suitable combination of all these variables is important to avoid trying different experimental parameters to find defects, ultimately accomplishing the goal with the smallest number of experiments and allowing inspectors to perform NDT more effectively [Haftka, et al., 1998].

In Chapter 3, shearography fringe prediction with finite element analysis is used to illustrate the optimization of NDT procedures by laser shearography on a plate made of acrylic and having a partial hole at the center.   To validate and demonstrate that the optimized experimental procedure is correct, shearography experiments are conducted on the same sample (the plate with a partial hole) based on optimized experimental procedure.

In addition, to verify the results of finite element analysis, the analytical and computational

solutions are compared on a simpler case – a plate with a through hole at the center because

the analytical solution of a plate with a partial hole is difficult to obtain.   To summarize,

the procedure of verification and validation of analytical, numerical, experimental solutions

on samples under test are shown in Figure 3.1
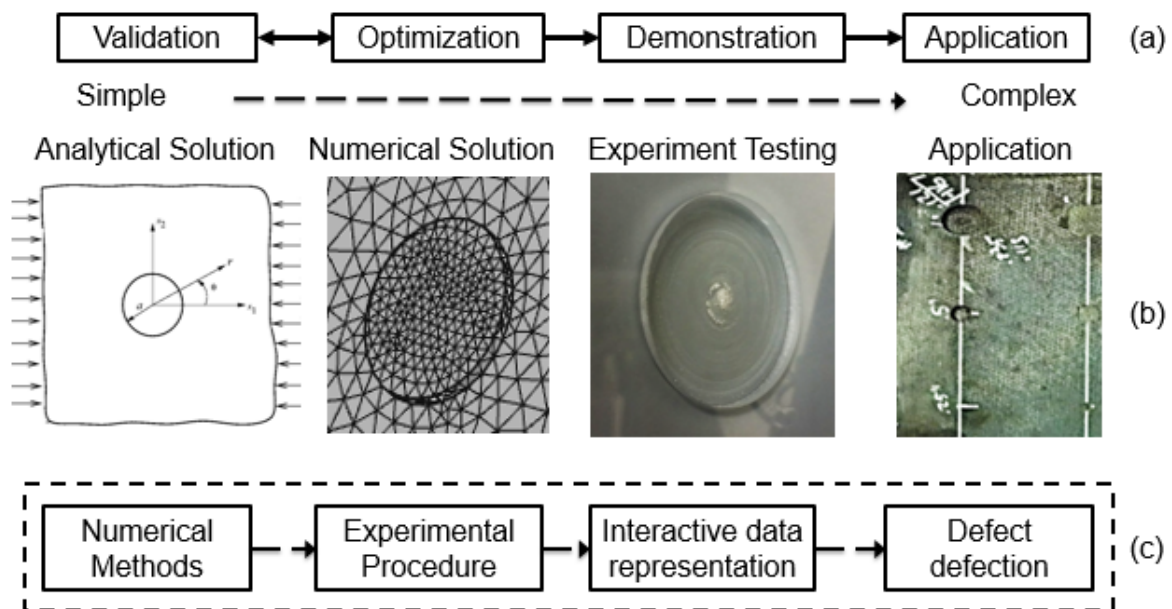
Figure 3.1.   Workflow to perform NDT by laser shearography: (a) the process from
validation to application while making use of analytical and computational methodologies;
(b) process applied to a specific case study; (c) numerical procedures are validated
analytically and applied to perform experimental procedures that are interactively utilized
to test components

Section 3.1 describes the verification of finite element analysis of a plate with a through

hole in compression and Section 3.2 describes the optimization and validation of shearography procedures to test a plate with a partial hole also subjected to compression.

3.1 Finite element analysis

Finite element analysis is used for estimating solutions to boundary value problems. In this methods, the object under investigation is divided into elements, each of which has simple user-defined geometry.   The elements are then linked by nodes, as shown in Figure 3.2.   Because of each element's simple geometry, the mechanical behavior of a sample—including strains, stresses, and displacements—can be calculated with highly accurate results.   We chose to combine finite element analysis (FEA) with shearography due to such benefits.   Based on NDT by laser shearography's principles, a deformation must be introduced to the sample under investigation and the displacement vector of the sample surface is joined with the sensitivity vector to determine the optical path difference.   Doing so is essential for determining the quality of the shearography wrapped phase, and as a result, for improving inspectors' understanding of how to apply the appropriate loading methods to achieve the desired deformation without damage to the sample.   With the results of the simulated deformation of the sample, the inspector would have a clearer idea of how to introduce the desired deformation during real testing [Kreis, 2005].
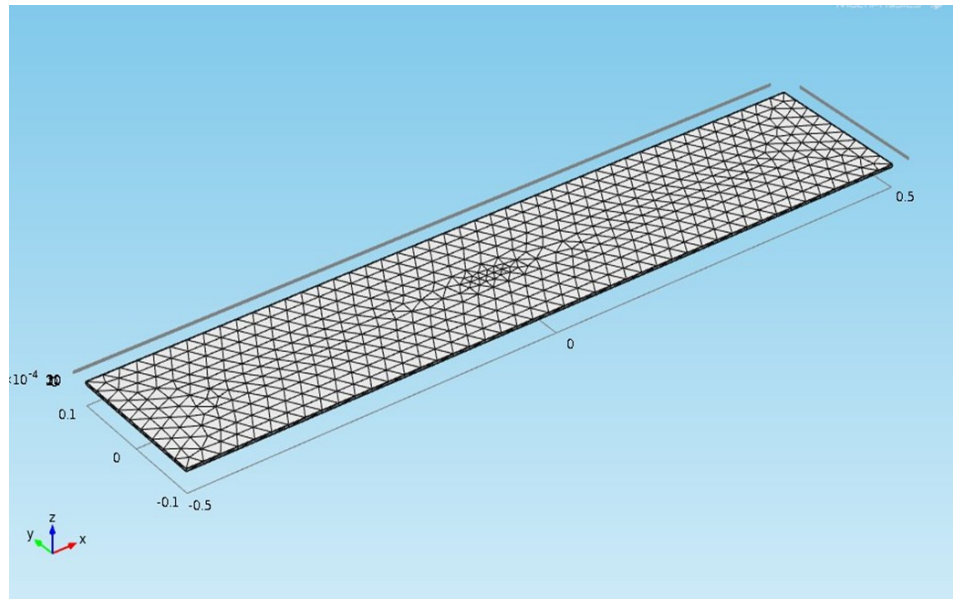
Figure 3.2.   Discretization of an aluminum plate sample in preparation
for Finite Element Analysis (FEA)

3.1.1 Verification of finite element analysis solutions by analytical solution: representative example

A very important issue relating to the FEA, or, in general, to any approximate solution, is the accuracy of the results [Pryputniewicz, 1994].   Verification of numerical solution is critical because the model built in FEA based on idealization and assumption.   To verify the accuracy of the FEA results, the analytical solution of a plate that has a through hole with compression loading compared with those obtained by FEA.   Figure 3.3 shows a schematic that illustrates the work flow of comparing FEA with analytical solutions.   We can either assume the geometry as an infinite plate and solve the problem analytically, or

approximate the geometry as a collection of "finite elements", and solve the problem

numerically [de Larminat et al., 1978; ANSYS Tutorial Website, 2014].
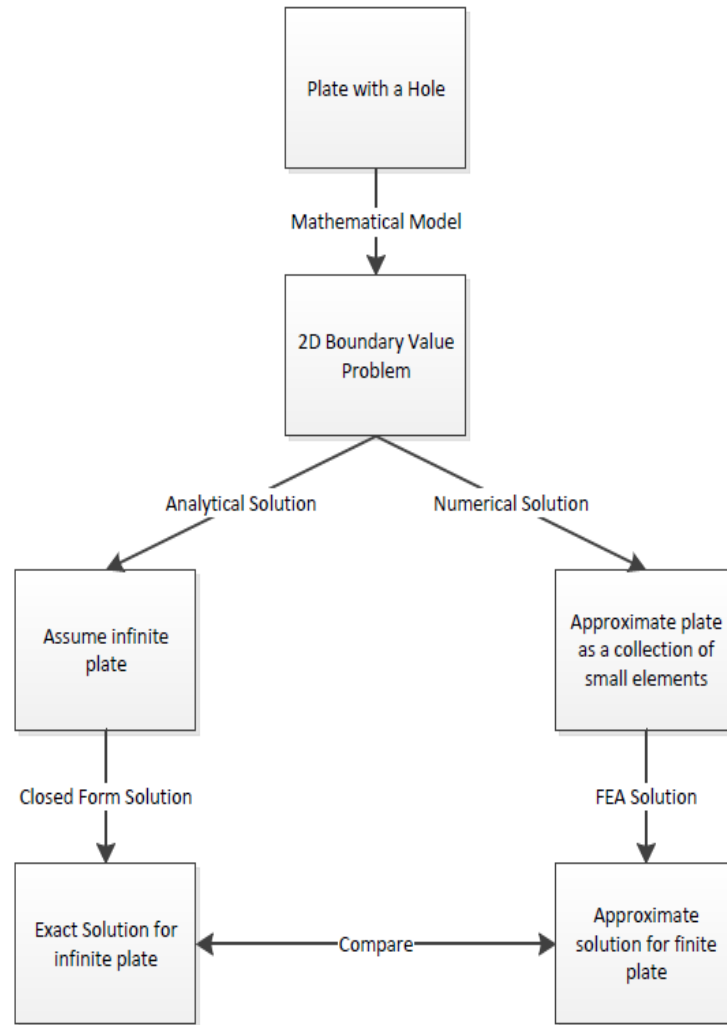
Figure 3.3.   A flow chart illustrating the comparison of analytical and numerical
approaches [ANSYS Tutorial Website, 2014]

In this Section, due to the current shearographic system is sensitive to displacements in the

direction of viewing, normal surface displacements around the circular hole are investigated.

The displacements are caused by subjecting the plate to an in-plane compressive load on the

order of 220 kPa.   Figure 3.4 shows the schematic of the plate with a circular hole in the
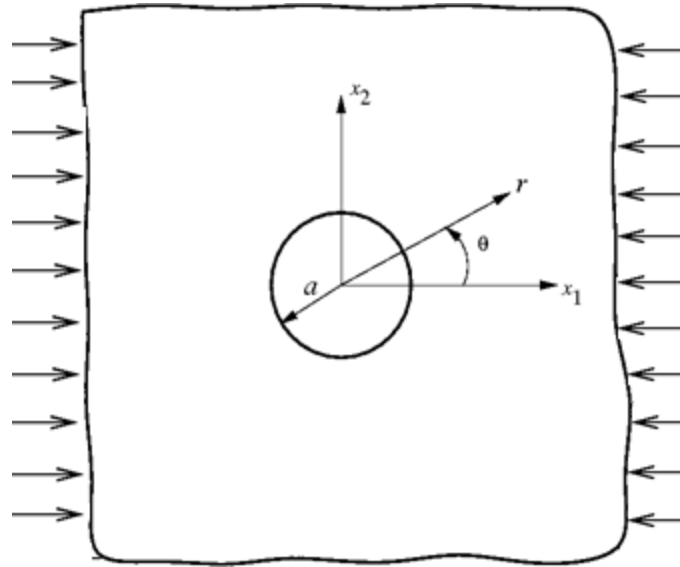
center.

Figure 3.4.   Schematic of the plate with a circular hole in the center subjected to un-
directional compression loading

For validation purposes, one dimensional out-of-plane displacement of a vertical cross-

section, from the center of the hole to the edge of the plate, is calculated by FEA using

COMSOL software and the analytical solution by applying elasticity theory [Maceri, 2010;

Chen et al., 2014; COMSOL, 2014].   For a large thin plate with a small circular hole at

the center, that is subjected to uni-axial compression , σ, the stresses (radial, circumferential

and tangential) around the vicinity of the hole are given in polar coordinates (r, θ) by the

following representations [Nagpal et al., 2011],

31

$$\sigma_{rr} = \frac{\sigma}{2}\left(1 - \frac{a^2}{r^2}\right) + \frac{\sigma}{2}\left(1 - \frac{a^2}{r^2}\right)\left(1 - \frac{3a^2}{r^2}\right)\cos 2\theta, \tag{32}$$

$$\sigma_{\theta\theta} = \frac{\sigma}{2}\left(1 + \frac{a^2}{r^2}\right) - \frac{\sigma}{2}\left(1 + \frac{3a^4}{r^4}\right)\cos 2\theta, \tag{33}$$

$$\sigma_{r\theta} = -\frac{\sigma}{2}\left(1 - \frac{a^2}{r^2}\right) - \frac{\sigma}{2}\left(1 + \frac{3a^2}{r^2}\right)\sin 2\theta, \tag{34}$$

where σ_{rr} is the radial stress, $\sigma_{\theta\theta}$ is the circumferential stress, and $\sigma_{r\theta}$ is the tangential stress. a is the radius of the circular hole and θ is the angle measured counter clockwise from x_1-axis. The normal surface displacement, W, can be calculated by [de Larminat et al., 1978]

$$W = -\frac{h\mu}{2E}(\sigma_{rr} + \sigma_{\theta\theta}), \tag{35}$$

where h is the thickness of the plate, E is the Young's Modulus, μ is the Poisson's ratio. By substituting Equation 32 and 33 to Equation 35, it is obtained that,

$$W = -\frac{h\mu}{2E}\left[\frac{\sigma}{2}\left(1 - \frac{a^2}{r^2}\right) + \frac{\sigma}{2}\left(1 - \frac{a^2}{r^2}\right)\left(1 - \frac{3a^2}{r^2}\right)\cos 2\theta + \right.$$

$$\left.\frac{\sigma}{2}\left(1 + \frac{a^2}{r^2}\right) - \frac{\sigma}{2}\left(1 + \frac{3a^4}{r^4}\right)\cos 2\theta\right]. \tag{36}$$

Dimensions of the plate of interests are 203.2 mm, 95.25 mm, and 4.76 m in length, width, and thickness, respectively, the diameter of the hole is 38.1 mm.

In comparison, a numerical solution to the above problem is obtained by using COMSOL software [COMSOL, 2014], shown in Figure 3.5.
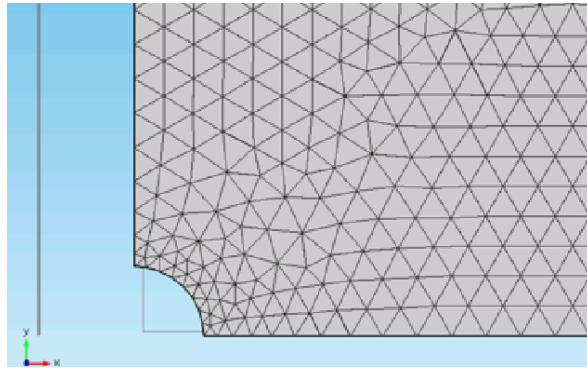
Figure 3.5.   Discretized zoomed-in view of the plate with the hole that is symmetrically modeled

The modules in COMSOL used for the analysis are: Structural mechanics module – Solid mechanics – stationary analysis.   Since the plate in COMSOL is symmetrically modeled as shown in Figure 3.5, the compressive load of 220 kPa is applied to the right edge of the geometry.   The left edge and bottom edge of the model are constrained with symmetrical boundary conditions.   To solve this problem using FEA, the geometry under investigation is divided into elements, typically triangles or quadrilaterals in two dimensions and tetrahedral or hexahedral in three dimensions [Bapat, 2011], as shown in Figure 3.6.
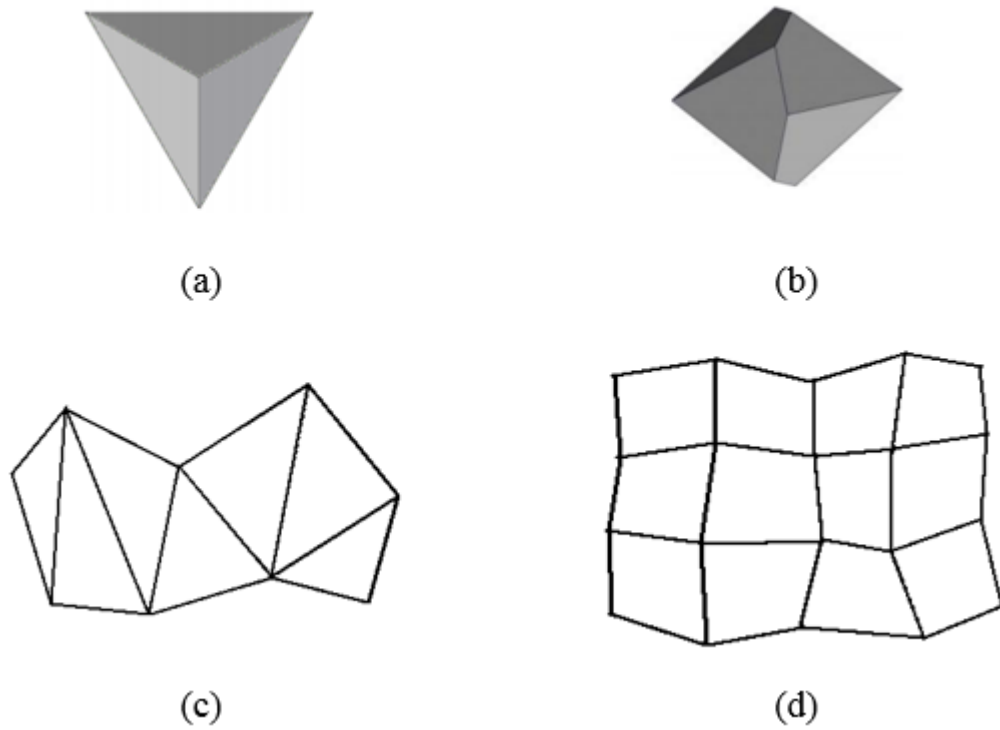
Figure 3.6.   Mesh element types: (a) tetrahedral element; (b) hexahedral element
(c) triangles element and (d) quadrilaterals element [Bapat, 2011]

In the models considered, tetrahedral elements are used and their size are defined by

assigning a minimum element size is in the order of 2×10^{-4}m.

Figure 3.7 shows the corresponding out-of-plane displacement of a vertical cross-

section from the center of the hole to the edge of the plate calculated by FEA and by the

analytical solution [Nagpal et al., 2012; ANSYS Tutorial Website, 2014].   Comparing the

analytical and FEA solutions of the out-of-plane displacements, it can be observed a good

agreement between both solutions.
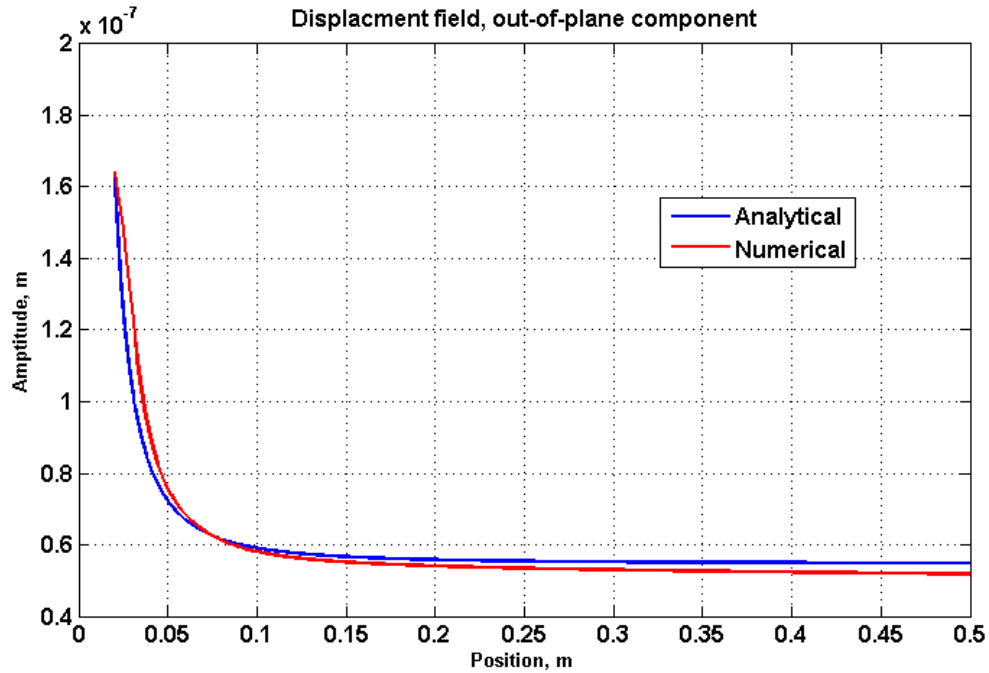
Figure 3.7.   Corresponding out-of-plane displacement results calculated by FEA and by analytical solutions

3.2 Validation and optimization of shearography procedures by use of fringe

prediction with FEA

Predicting the shearography fringe patterns as a function of sample displacement or deformation is useful for several reasons: this prediction can aid in the planning phase of laser shearography measurement, in which an optimized laser shearography setup

arrangement must be designed.   Predicting the fringes also allows us to verify that the system's sensitivity chosen produces fringes of sufficient but not overly high density [Kreis, 2005].   In addition, by viewing the simulated fringe patterns, the inspector would have a clearer idea of how to introduce the suitable loading methods to obtain desired deformation during a real test.

In this Section, a hybrid approach for optimizing the shearography experimental procedures by fringe prediction with finite element analysis is discussed.   In addition, experimental measurements of a plate with a partial hole is conduct by laser shearogrpahy in order to validate the predictions, so that the optimized experimental procedure could be applied to effectively perform NDT.

3.2.1 Fringe prediction

To simulate the expected fringe patterns produced by laser shearography procedures, a fringe prediction algorithm based on FEA is developed by using the corresponding governing equations described in Chapter 2.   The algorithm simulates the expected fringe patterns based on the experimental setup arrangement, sensitivity vector K (x, y, z), and the deformations of the object under investigation; Appendix A includes MATLAB code to perform fringe prediction.

According to the equations in Chapter 2, by defining the wavelength of the laser source

and by simulating displacements of the target, the expected shearography wrapped-phase

pattern can be determined by Equation 8 with a given setup arrangement and given loading

methods.   A typical setup arrangement is shown in Figure 3.8.
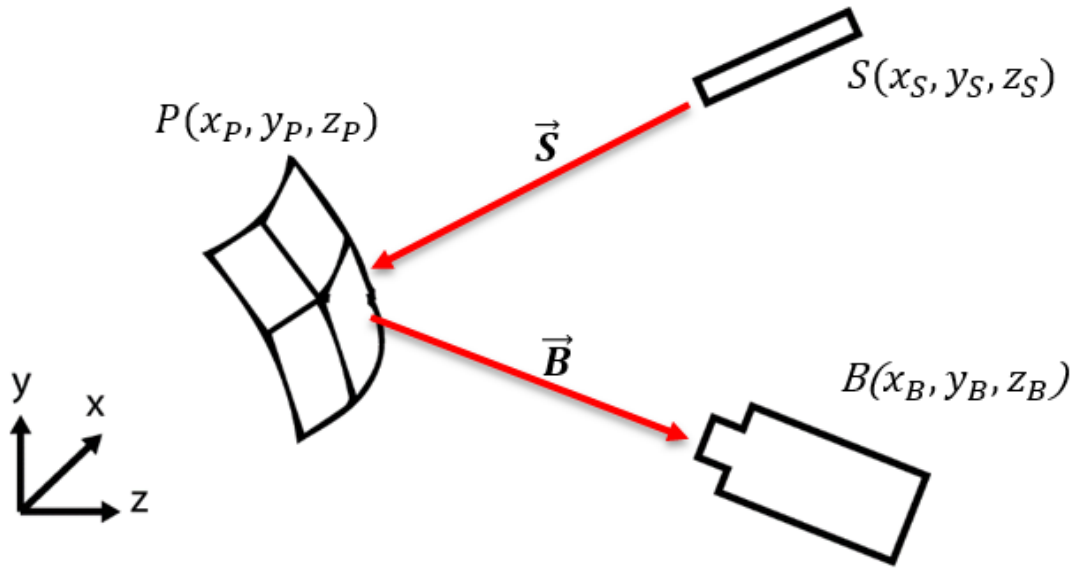
Figure 3.8.   Illumination and observation geometry showing the locations
of the point of the illumination, S, the point of observation, B, and the
optical path from the point of illumination to a point on the surface of the
object under investigation, P, and to the point of observation

According to Figure 3.8, the sensitivity vector can be defined with

$$\boldsymbol{K}(x, y, z) = \boldsymbol{B}(x, y, z) - \boldsymbol{S}(x, y, z), \tag{37}$$

where $\boldsymbol{S}$ is the illumination vector and $\boldsymbol{B}$ is the observation vector. $B(x, y, z)$ and

$S(x, y, z)$, for the point P (x_p, y_p, z_p), are computed with

$$S(P) = \begin{bmatrix} S_x(P) \\ S_y(P) \\ S_z(P) \end{bmatrix} = \frac{1}{\sqrt{(x_P - x_S)^2 + (y_P - y_S)^2 + (z_P - z_S)^2}} \begin{pmatrix} x_P - x_S \\ y_P - y_S \\ z_P - z_S \end{pmatrix} , \tag{38}$$

and

$$B(P) = \begin{bmatrix} B_x(P) \\ B_y(P) \\ B_z(P) \end{bmatrix} = \frac{1}{\sqrt{(x_B - x_P)^2 + (y_B - y_P)^2 + (z_B - z_P)^2}} \begin{pmatrix} x_B - x_P \\ y_B - y_P \\ z_B - z_P \end{pmatrix} . \tag{39}$$

By substituting Equations 37, 38 and 39 to Equation 7, the phase difference between the object before and after deformation can be calculated as

$$\Omega = \frac{2\pi\Delta x}{\lambda} \frac{\delta L(x,y,z)}{\delta s} K(x,y,z)$$

$$= \frac{2\pi\Delta x}{\lambda} \frac{\delta L(x,y,z)}{\delta s} \begin{bmatrix} B_x(P) - S_x(P) \\ B_y(P) - S_y(P) \\ B_z(P) - S_z(P) \end{bmatrix}$$

$$= \frac{2\pi\Delta x}{\lambda} \frac{\delta L(x,y,z)}{\delta s} \left[\frac{1}{\sqrt{(x_B - x_P)^2 + (y_B - y_P)^2 + (z_B - z_P)^2}} \begin{pmatrix} x_B - x_P \\ y_B - y_P \\ z_B - z_P \end{pmatrix} - \right.$$

$$\left. \frac{1}{\sqrt{(x_P - x_S)^2 + (y_P - y_S)^2 + (z_P - z_S)^2}} \begin{pmatrix} x_P - x_S \\ y_P - y_S \\ z_P - z_S \end{pmatrix} \right] . \tag{40}$$

According to Equation 40, the optical phase difference between the sample before and after deformation can be calculated by a given displacement field, sensitivity vector $K\ (x, y, z)$, the wavelength of the light source, and the amount of shear. The corresponding shearographic modulation fringes can be calculated as

$$I = \cos(\Omega). \tag{41}$$

3.2.2 Representative fringe prediction results and experimental validations

In this Section, fringe prediction with FEA is used to optimize the NDT procedure by laser shearogrpahy of a plate made of acrylic that has a partial hole at its center. Shearographic experiments are performed to validate that the design of the experimental procedure could yield the desired results from experiments and could result in speeding up NDT procedures.

Figure 3.9 shows an FEA model of this plate. To obtain deformation data to be used in fringe prediction some type of loading is required. The criteria to identify appropriate loading from fringe prediction varies from case to case depending on the geometry and the mechanical properties of the sample being tested. In addition, the corresponding costs of the loading mechanism need to be taken into consideration. The main objective is that the chosen loading methods are able to produce appropriate local strains around the defects, which can be identified as they generate irregular fringes on the sample. Also, the desired loading methods need to be easily applied and the cost of the corresponding loading mechanism as inexpensive as possible. For these measurements, the plate undergoes first, acoustic loading and then, in-plane loading, and consequently, corresponding fringe patterns are predicted for each case. Simulations are performed in COMSOL and the dimensions

of the sample are 203.2 mm, 95.25 mm, and 4.76 mm for length, width, and thickness, respectively, which are the same as the dimensions of the plate used in the experiments [COMSOL, 2014].   The diameter of the hole (defect) is 38.1 mm and its depth is 3.175 mm.
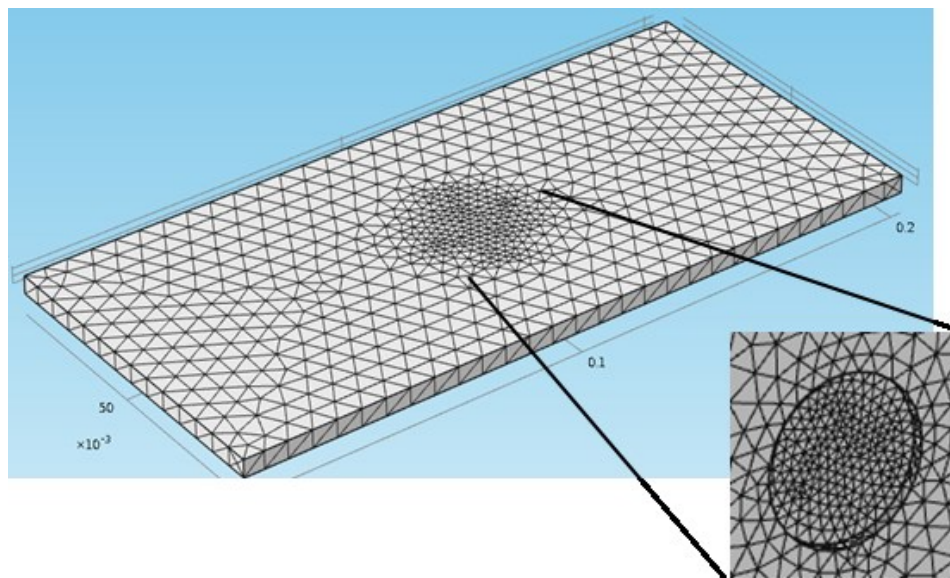
Figure 3.9.   FEA mesh of a plate with a partial hole having the dimensions of 203.2 mm for the length, 95.25 mm for the width, and 4.76 mm for the thickness.   Diameter of the partial hole is 38.1 mm and its depth is 3.175 mm

3.2.2.1 FEA and fringe prediction results

Acoustic loading simulations are performed using Eigen frequency analysis.   The modules in COMSOL used for the analysis are: Structural mechanics module – Solid mechanics – eigenfrequency.   The overall size of mesh is selected based on the

convergence of the solutions while mesh refinements are used locally in the vicinity of concentrated reactions to have accurate results. Tetrahedral elements are used and the size of the elements are defined by assigning the minimum element size of 2×10^{-4}m while the boundary conditions are set by constraining the two short edges in the model. Figure 3.11 shows the predicted shearographic fringe patterns for the first six modes of vibration of the plate corresponding to the model shown in Figure 3.10.
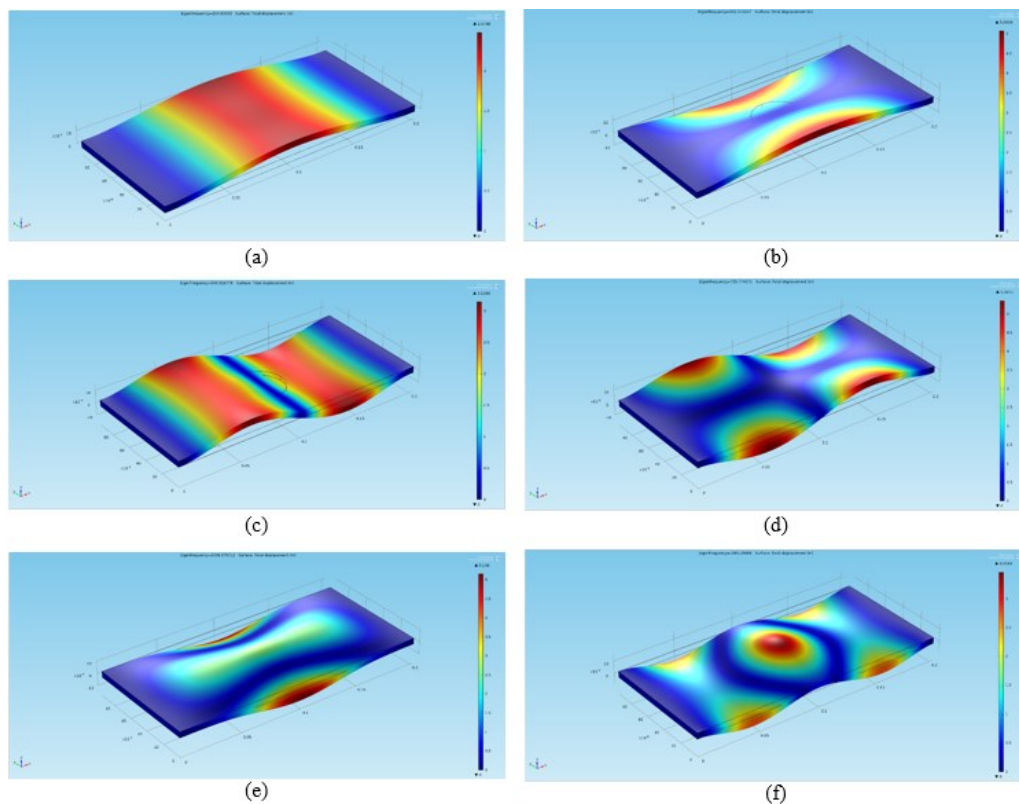
Figure 3.10.   Deformation of an acrylic plate with a partial hole at the center corresponding to the first six modes of vibrations as obtained with FEA with COMSOL

By defining the location of light source and shearography head, corresponding shearography fringes can be calculated by using Equations 40 and 41 with simulated displacement field of the object obtained by FEA. As shown in Figure 3.11, the defect (partial hole) is either not detectable with acoustic loading or the acoustic level of excitation is too high. Therefore, it is necessary to change the loading condition in order to detect the defect.
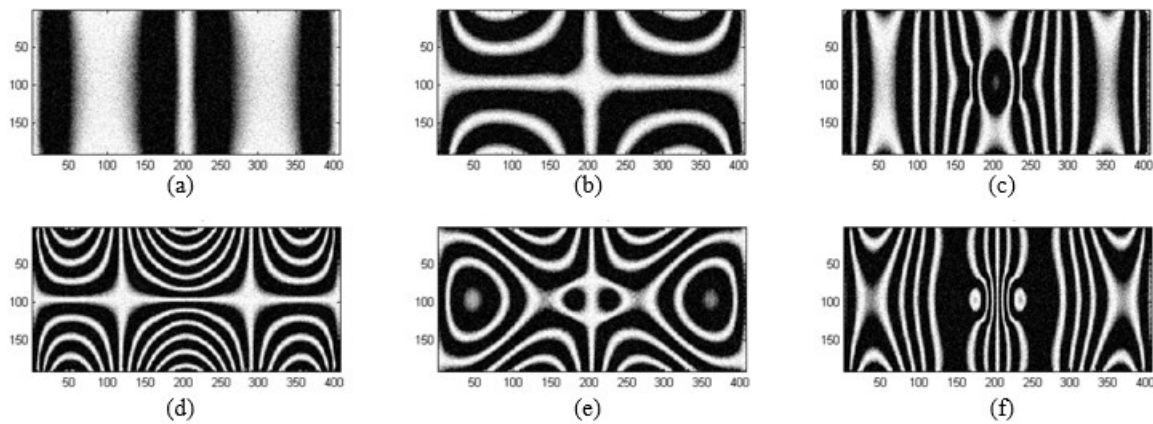
Figure 3.11. Prediction of shearographic fringes from the FEA results (that are shown in Figure 3.10): (a) 205Hz; (b) 332Hz; (c) 545Hz; (d) 735Hz; (e) 1038Hz; and (f) 1085Hz, respectively

Uniaxial compression loading of 220 kPa is simulated next. The element's size and type are the same as those used for acoustic loading simulations. In this case, as shown in Figure 3.12 and 3.13, the simulation results indicate that using compression loading, inspectors could locate a partial hole (defect) with laser shearography in a more effective

42

way than with vibrational loading.
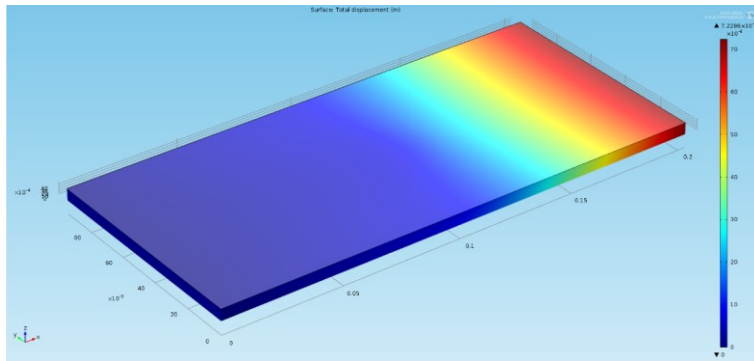
Figure 3.12.   FEA results of deformation of an acrylic plate with a partial hole at the center subjected to compressive load
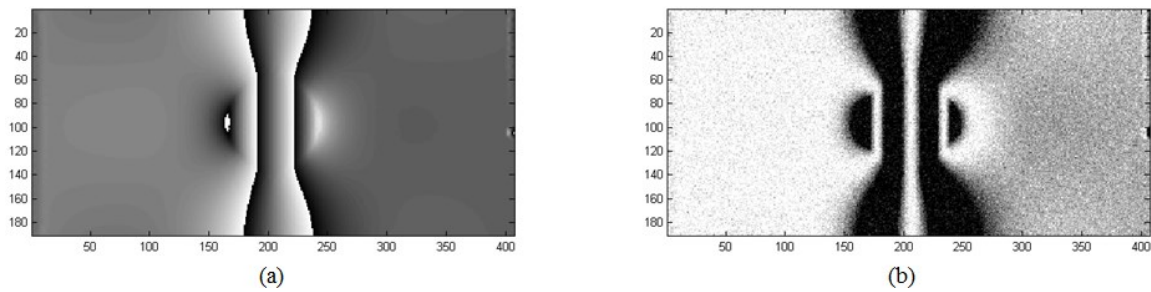
Figure 3.13.   Prediction of shearographic fringes from the FEA results (that are shown in Figure 3.12): (a) wrapped optical phase; (b) corresponding shearography intensity fringes

3.2.2.2 Experimental measurements for validating fringe prediction results

The corresponding experimental setup by using shearography is built based on the optimized experimental procedure to inspect the acrylic plate with compression loading. The dimensions of the sample, as shown in Figure 3.14, are the same as in the model analyzed by the FEA, Section 3.3.2.1.
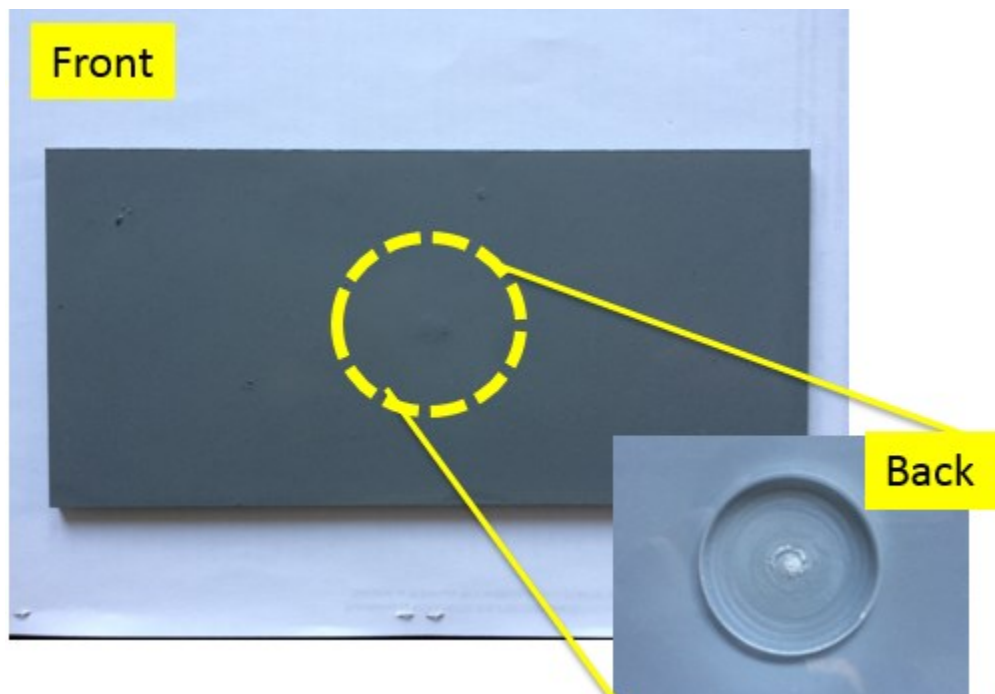
Figure 3.14.   A plate made of acrylic with a partial hole under testing; the dimensions of the sample are a length of 203.2mm, width of 95.25mm, and thickness of 4.76mm. Diameter of the hole is 38.1m and its depth is 3.175mm

In the experimental setup, shown in Figure 3.15, the sample under investigation is

compressed from both sides with two flat plates and with one of these plates mounted to a linear stage to apply controlled load to the sample.   The arrangement of the experimental setup is shown in Figure 3.15a.   The projector shown in Figure 3.15 is used for projecting the shearogrpahy results back onto the sample for the operators to clearly identify the a state of deformations, see Chapter 4.
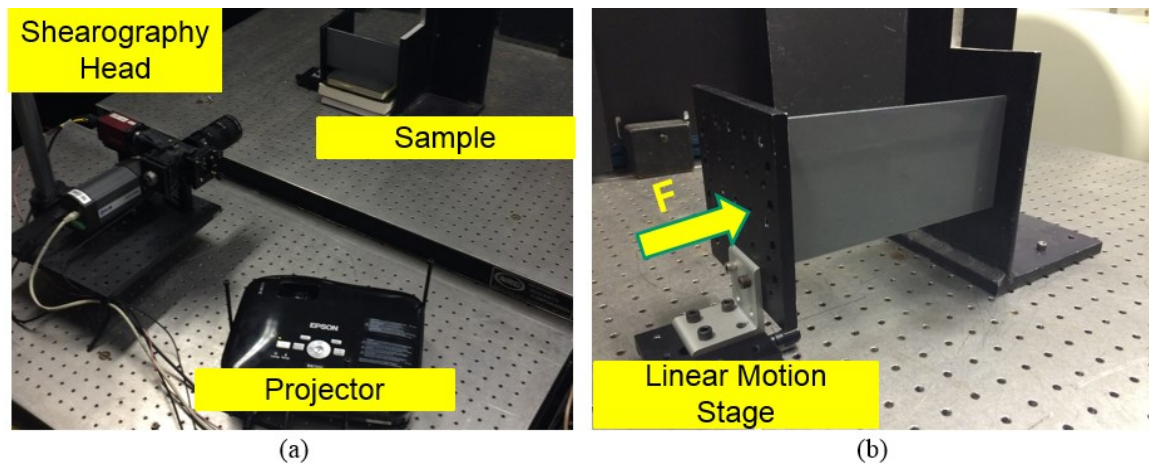
Figure 3.15.   A plate with a partial hole under compression load testing: (a) an overview of the experiment setup consisting of shearography head, sample, and multimedia projector; (b) zoomed-in view to show the method to apply the load

Figure 3.16 shows the representative results of NDT by laser shearography.   From the results shown in Figure 3.16b, the edge of the defect can be clearly detected, which demonstrates that the experiment procedure optimized by the hybrid technique of combining fringe prediction and FEA reduces the number of experiments and number of loading methods.   This results in a more effective procedure to evaluate and perform NDT testing of components.

<div align="center">(a)</div>

<div align="center">(b)</div>
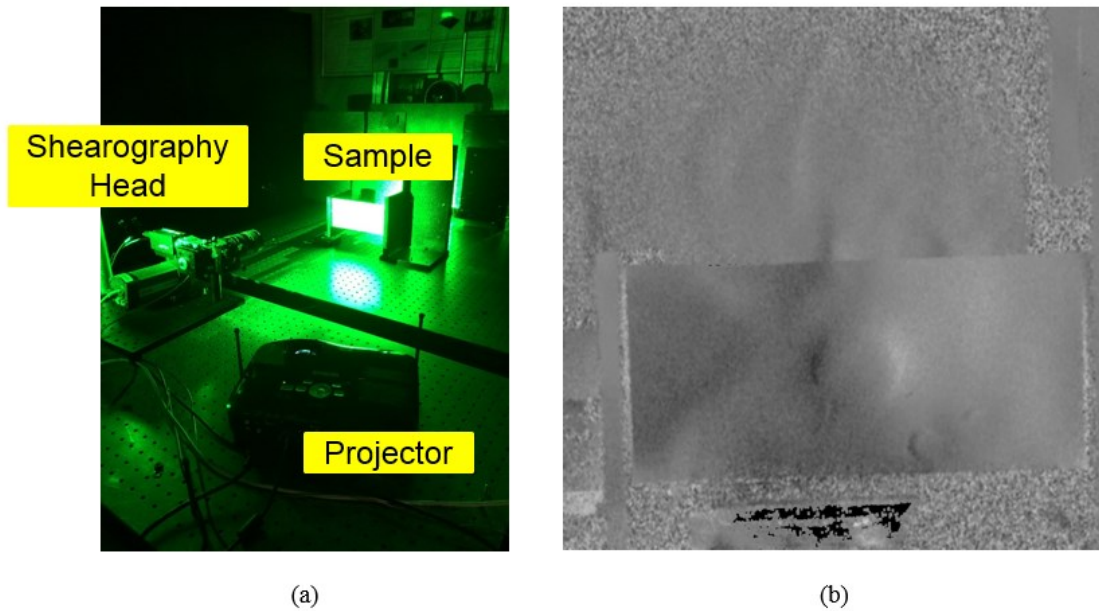
Figure 3.16.   A plate with a partial hole under shearographic testing: (a) experiment setup; (b) wrapped optical phase that enables the identification of the defects.   The use of the projector shown in (a) is discussed in Chapter 4

Figure 3.17 shows the comparison of results between fringe prediction and actual shearography measurements.   After processing both data sets, which included the use of spatial filtering and data normalization, the data were quantitative compared and the results shown good agreement. This indicates that the use of fringe prediction with FEA could help inspectors to perform shearography experiments more efficiently.
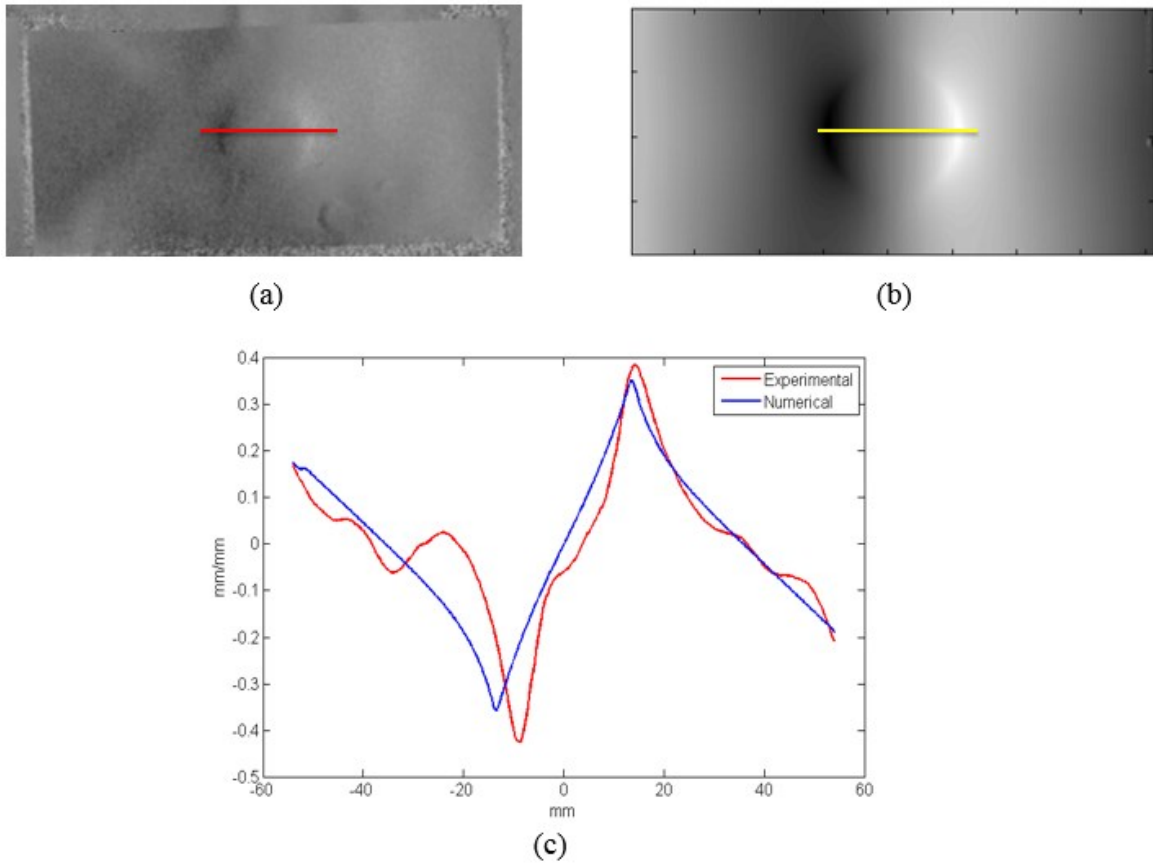
Figure 3.17.   The comparison between fringe prediction with FEA and experimental results: (a) phase map obtained by experimental measurements with shearography; (b) corresponding post-processed phase map obtained by simulations; and (c) representative cross sections of (a) and (b), respectively

4. Visualization of shearography data on samples under testing

By visualizing the results of laser shearography, identification of the defects on the actual surface under test can be performed with high accuracy [Fantin, et al., 2012; Chen, et al., 2014]. For this purpose, we introduce a multimedia projector at the end of the shearography workflow in order to project the measurements onto the real surface of the sample under testing. Therefore, allowing us to mark the defects on the real sample with greater ease. Introducing a projector to the shearography setup will improve engineers' ability to identify the location of defects on real samples.

In order to visualize shearography results on the sample under testing, the image captured at the shearography camera's coordinates needs to be transferred to the coordinates at the projector's location. In other words, to project the shearography results using the multimedia projector, geometric transformations (which define the spatial relationships between different viewing geometry) need to be determined. A calibration procedure needs to be performed in order to obtain the geometric transformations [Gonzalez et al., 2004; Zervas, 2011; Fantin, et al., 2012].

4.1 Image registration techniques

The process of aligning two or more images of the same scene captured by different perspectives is called image registration. Typically, one image is called the base image

and is considered as a reference to which the other images, called input images, are compared.   The aim of image registration is to bring the input image into alignment with the base image by applying a spatial transformation to the input image.   A typical image registration procedure is shown in Figure 4.1
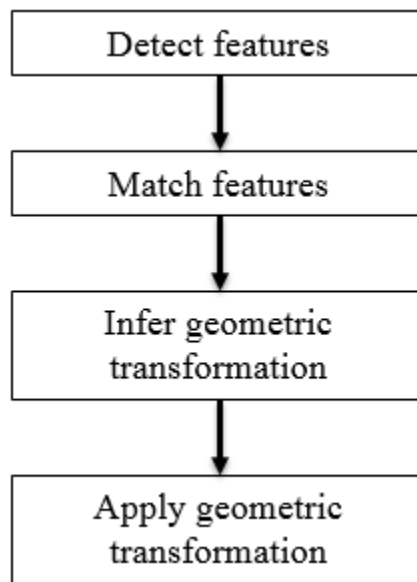
Figure 4.1.   Image registration procedure used to project shearography
results onto samples under test

In the procedures for detecting and matching features, shown in Figure 4.1, an image feature is any part of an image that can be identified and located in both images.   Features can be points, lines, or corners.   Matched–feature pairs are selected and a geometric transformation function is inferred, which maps the features in one image on the locations

of the matching features in the other. Suppose that (w, z) and (x, y) are two spatial coordinate systems, where (w, z) is input space and (x, y) is output space, a geometric coordinate transformation is defined that maps input space points to output space points,

$$(x, y) = T\{(w, z)\}, \tag{42}$$

where T is called a forward transformation. If T has an inverse transformation, then the inverse maps output space points to input space points

$$(w, z) = T^{-1}\{(x, y)\}, \tag{43}$$

where T^{-1} is the inverse transformation. After inferring transformation function based on the selected matched–feature pairs, the transformation function is used to align one image with the other to complete the image registration process [Gonzalez et al., 2004; University of Dayton, 2014]. MATLAB Image Processing Toolbox (IPT) functions are used to realize the image registration process. The procedure of using IPT to conduct image registration is illustrated in Figure 4.2 [Matlab, 2014].
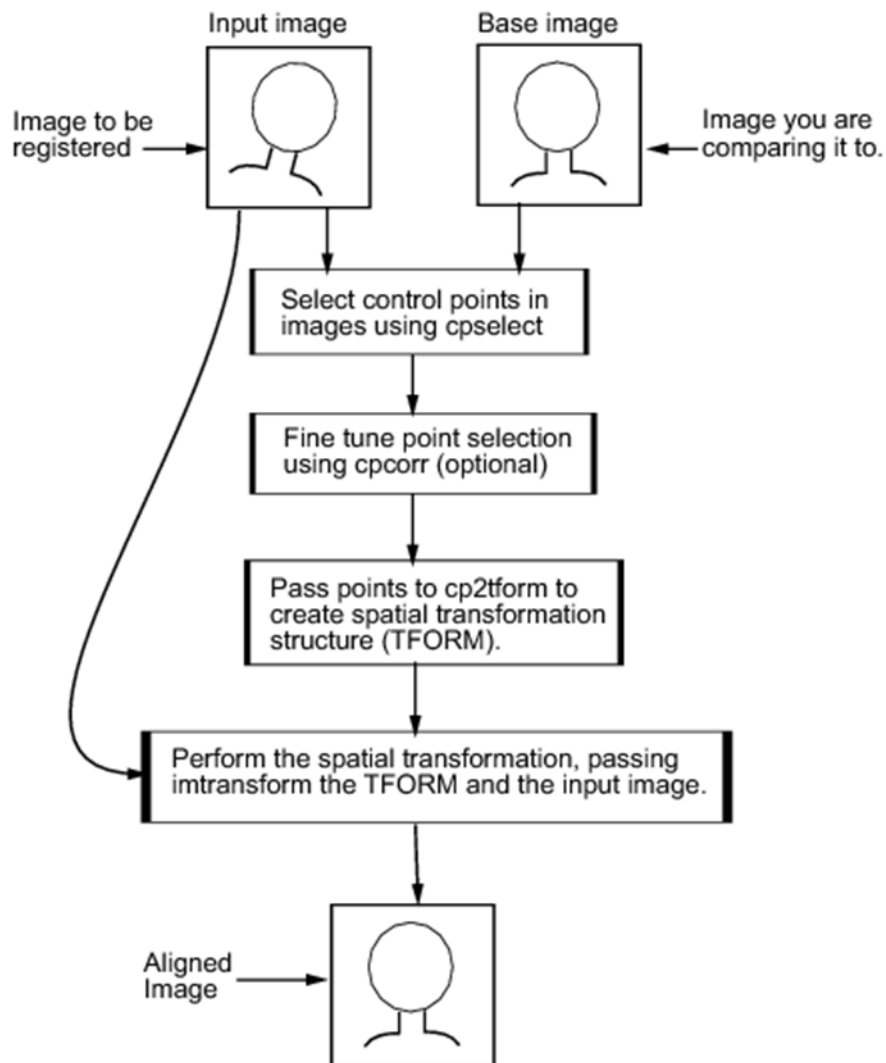
Figure 4.2.   Image registration process illustration with Matlab [University of Dayton, 2014]

To accomplish the image registration process in Matlab (as shown in Figure 4.2), first both input and base images are read in MATLAB.   Then, the image processing toolbox function (called the Control Point Selection Tool) is used to manually select matched–feature pairs in both images.   The tool provides several useful functions, such as zoom,

pan and scroll, which help users to easily navigate large images.   Once selected pairs have been identified and matched, a function called *cp2tfrom* is used.   The function, provided by IPT, is to infer the geometric transfer function based on the matched points.   After determining the transformation function, the *tfrom* function is applied to align the input image to the reference image, finalizing the image registration process.

In our case, the input image is the image recorded from the shearography camera, and the base image is the one projected by the multimedia projector.   We need to then register the image of shearography results to the image that will be projected by the multimedia projector.   The transformation matrix, which is the relationship between the shearography setup coordinate and the multimedia projector coordinate, is then applied to transfer the coordinates of the shearography results to the projector [University of Dayton, 2014].

4.2 Projector calibration

We developed a projector calibration algorithm to obtain the transformation matrix by realizing image registration techniques.   The related MATLAB code is included in Appendix B.   Once the location of the multimedia projector and the shearography system setup are determined, the relationship between the two coordinates is fixed.   As a result, the calculation of the transformation function can be separated from other experiments. This allows us to calculate the transformation function between the two locations by

introducing a simple image generated by a computer, making it more manageable for users

to manually select corresponding pairs of points.   The workflow for projector calibration

is shown in Figure 4.3.
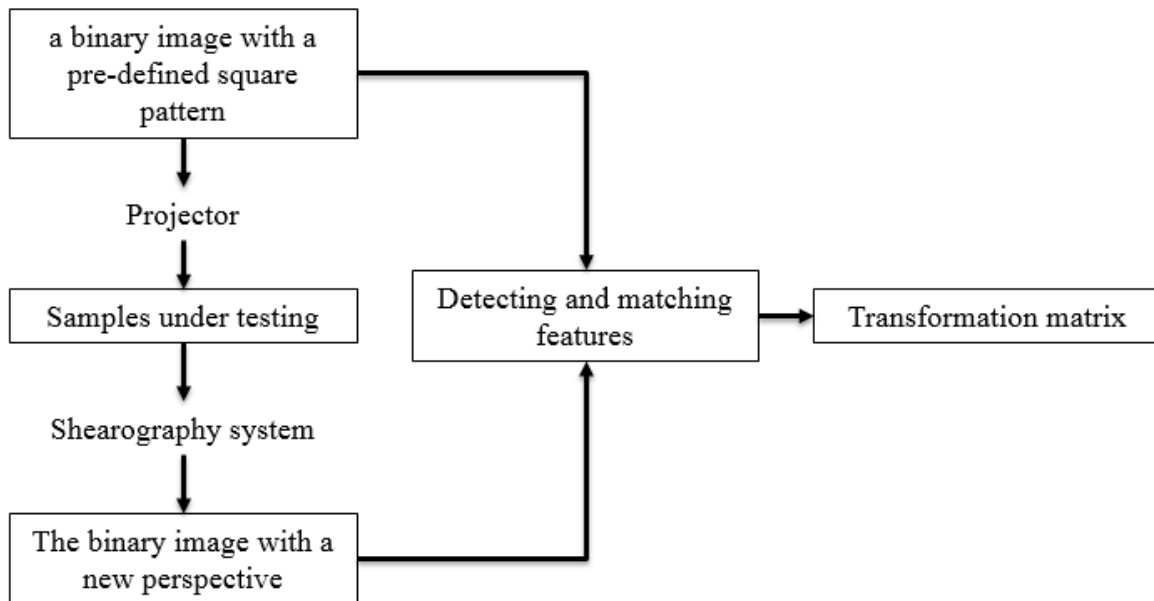
Figure 4.3.   Workflow of the projector calibration procedure to determine the
corresponding image transformation matrix

Based on the workflow shown in Figure 4.3, a binary image with a square pattern for

the base image is used for the purpose of alignment.   The binary image is projected by the

multimedia projector to the samples under testing.   Then, the shearography system's

camera is used to capture the image that the projector displays.   The image captured by the

shearography system's camera is the same binary image but from a new perspective, and is

called the input image.   Figure 4.4 shows both the base image and the input image.

(a)   (b)
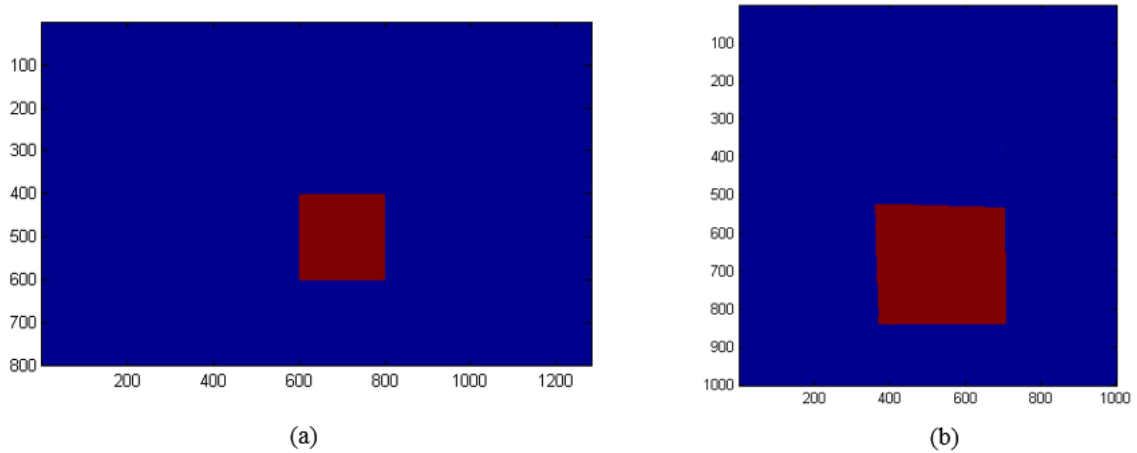
Figure 4.4.   Calculating the image transformation function: (a) a computer-generated
binary square pattern image used for image registration; (b) the base image projected by
the multimedia projector and captured by the camera of the shearography system

Based on these two images, the transformation function between the locations of the

projector and the shearography system can be calculated by selecting the number of control

points.   One pair of control points includes two points located at the same feature location

in these two images.

In our procedure, as a binary square pattern is used, four corners are used as the same

features in both images.   We can compare and select pairs of points by comparing the two

images in detail, meaning the image can be zoomed into until we select the preferred control

points, as shown in Figure 4.5.

54
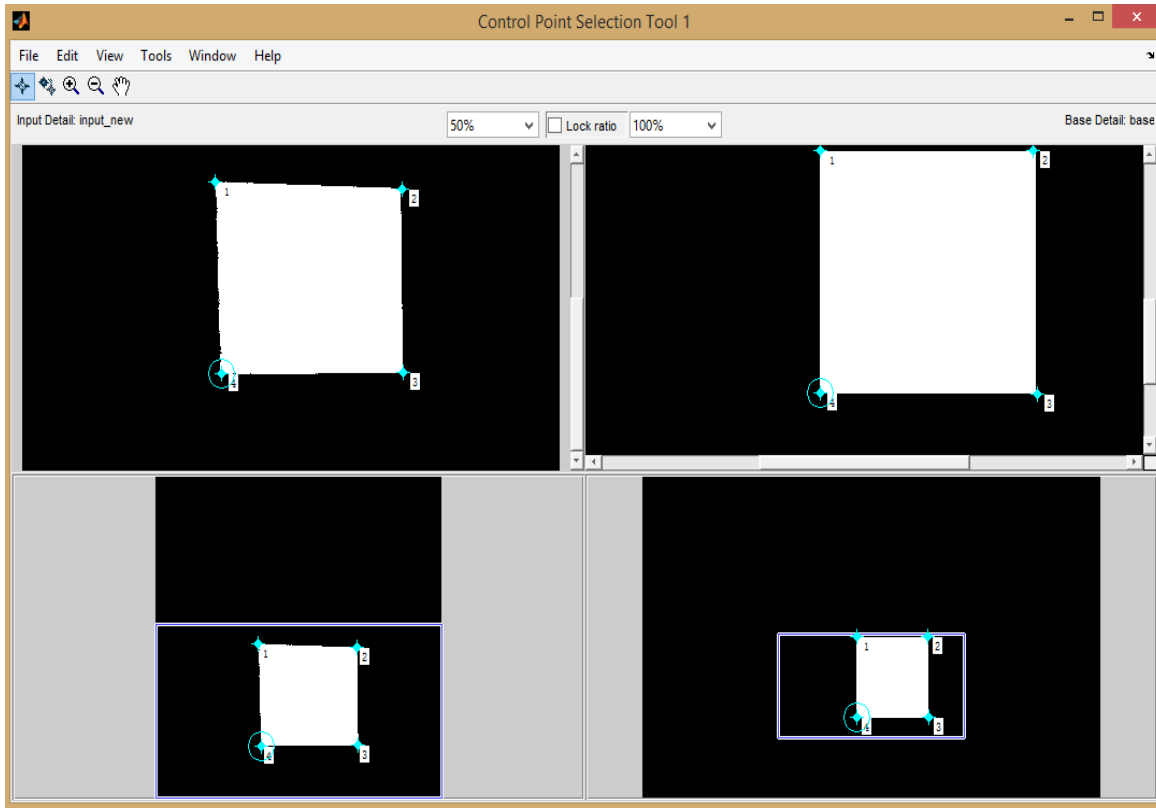
Figure 4.5.   Screen shot of the Control Point Selection Tool in MATLAB: the bottom left image is the one captured by the shearography system and the bottom right image is the one displayed by the multimedia projector; the top left and top right are the corresponding zoomed-in versions

Four point-pairs are selected during this process.   A cross-correlation function also can be used to fine tune the control point pairs.   Using the selected point-pairs and Equations 42 and 43, the transfer function (which is related to the coordinate differences between the shearography setup and the projector) can be determined.

4.3 Procedure of projecting shearography results on samples under test

Once we introduce the transfer function from the binary square pattern, we can apply

the transfer function to map the shearography results to the coordinates of the projector.

Figure 4.6a shows the experimental shearography results obtained in Section 3.2. After

applying the transfer function to the results, Figure 4.6b, the new registered image based on

the locations of the shearography system and projector is computed and is ready to be used

for projection onto the actual sample under test.

(a)   (b)
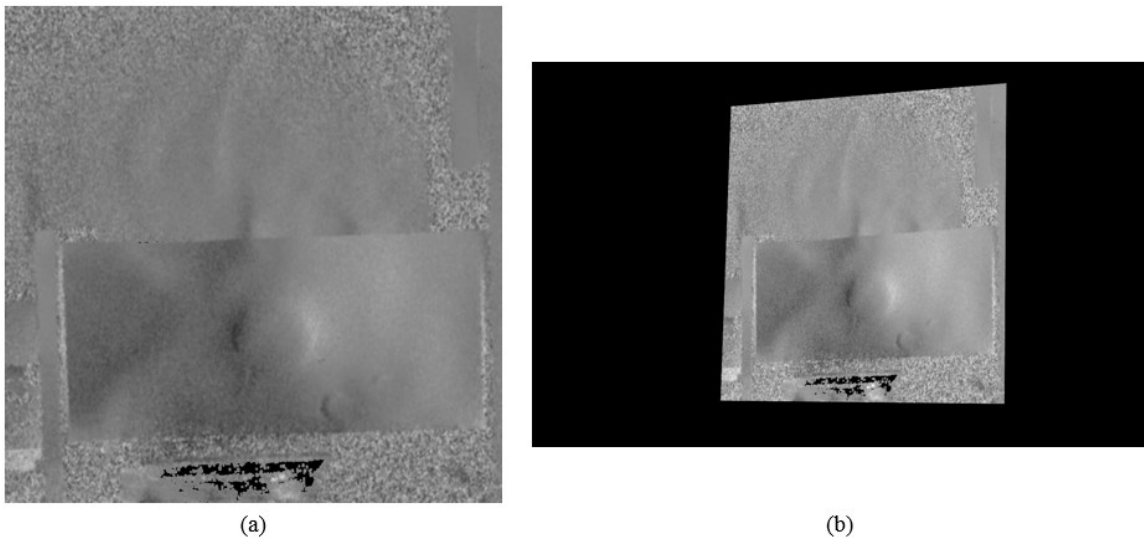
Figure 4.6.   Image registration results: (a) the experimental shearography results of
Section 3.2; (b) corresponding registered image based on the locations of the shearography
system and projector

Figure 4.7 shows the re-projection of the new registered shearographic results onto the

sample's surface in order to localize the defect on the sample.
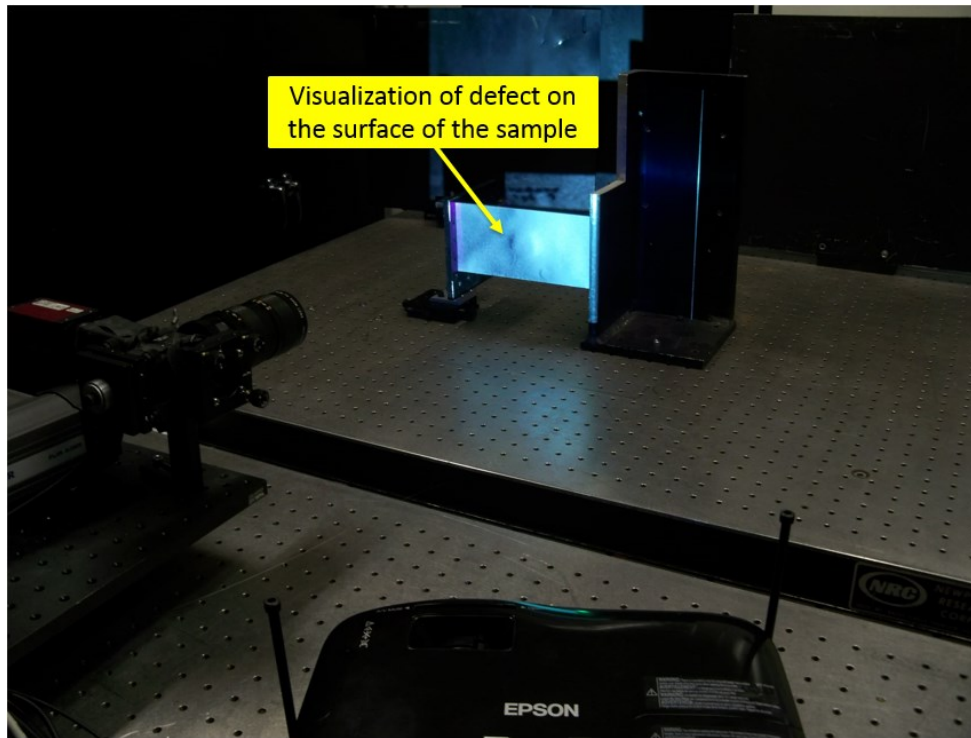
Figure 4.7.   Projection of the shearography results onto the actual sample under test

5. Representative applications

5.1 NDT of a composite panel

One common application of NDT using shearography is in the aerospace industry, where NDT is used to analyze the integrity of composite panels. Because of their high strength to weight ratio, composite panels are widely used in the aerospace industry. However, in some cases, they can be subject to delaminations due to impact or shock—a critical issue because this can lead to failure of the components. When applying a load, a delaminated region will exhibit strain anomalies compared with healthy regions. Shearography can make the location of delaminations visible through the identification of the delaminations-induced strain anomalies, which are translated into anomalies in the fringe pattern, even if they are below the surface because they still affect the surface deformation [Hung, 1996; Francis et al., 2010].

In this Section, we present the representative results of using laser shearography to detect delaminations in a composite panel. The experiment system setup and imaging processing results are presented. A view of one of our shearography implementation is shown in Figure. 5.1. The system consists of a shearography optical head, thermal loads, and the object under investigation [Chen et al., 2014].
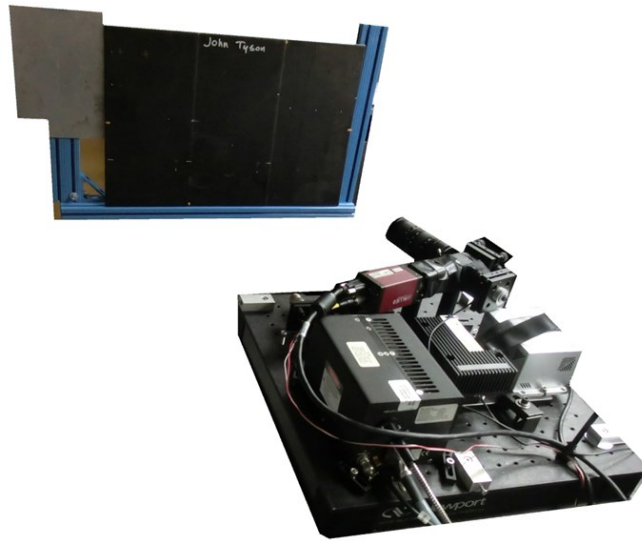
Figure 5.1.   The shearography system aimed at a composite panel

The optical head's measurements were made with an out-of-plane displacement gradient sensitive shearography system, located at a working distance of 1.8m from the panel.   The object illumination for shearography is provided by a pulsed laser with pulse energy of 0.2mJ with a wavelength of 532nm.

To detect irregularities or defects in an object using shearography, some type of loading is required.   For these measurements, tensile and compressive loading can cause damage to the sample and acoustic loading requires high input energy to highlight defects. Therefore, thermal loading is chosen to perform NDT on the composite panel with specific known defects, as shown in Figure 5.2.

| (a) | (b) |
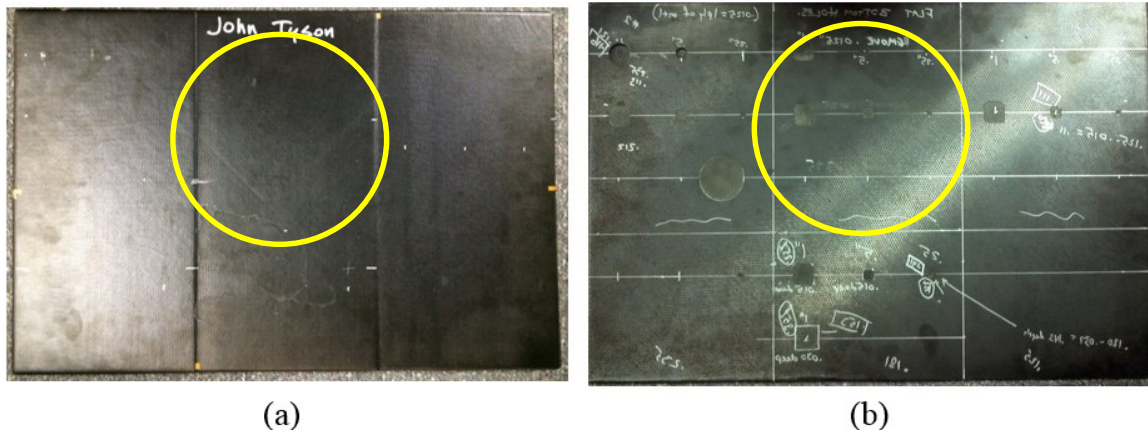
Figure 5.2.   Sample of interest with marks showing known defects to be investigated. Dimensions of the sample are: length of 692 mm, width of 457 mm, and average thickness of 4mm

A region of the surface of the panel is selected with an area of approximately 0.5m^2. A delamination has been labeled with a yellow circle in the center of the panel in Figure 5.2.—the delamination was artificially made for the purpose of testing.

Thermal loading was induced by means of heating lamps located behind the object of interest and applied evenly over the back surface of the object manually.   As shown in Figure 5.3, to thermally load the panel, three 250W Philips heating lights (Red R40) are mounted at a distance of 5cm behind the panel.   Each measurement induces a 3-second period of thermal loading, followed by 5 seconds of cooling time.   The processed wrapped phase map is shown in Fig. 5.4a, and the unwrapped phase map is shown in Fig. 5.4b. The damage locations can clearly be seen in the shearography results.
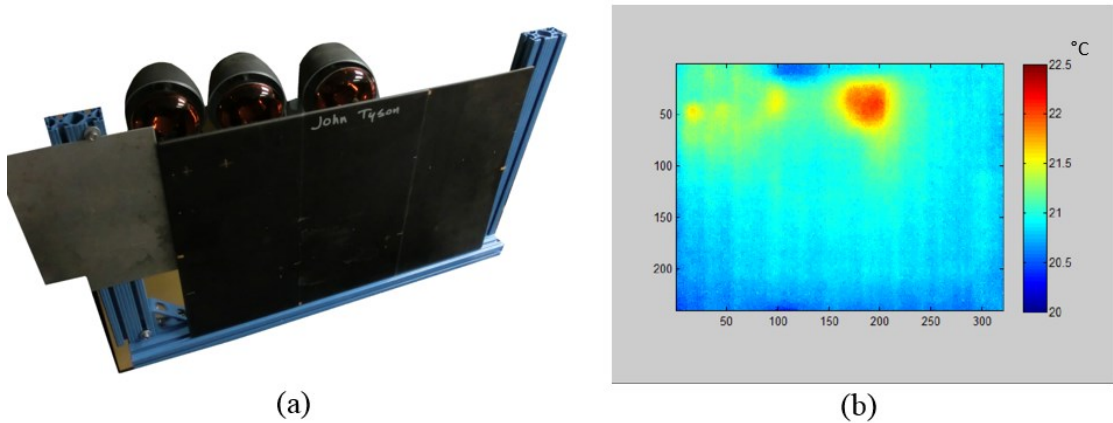
Figure 5.3.   NDT of a composite panel: (a) sample subjected to thermal excitation by an incandescent source; and (b) thermal field measured by an IR camera showing a maximum temperature difference of 2.5 ºC within the loaded panel
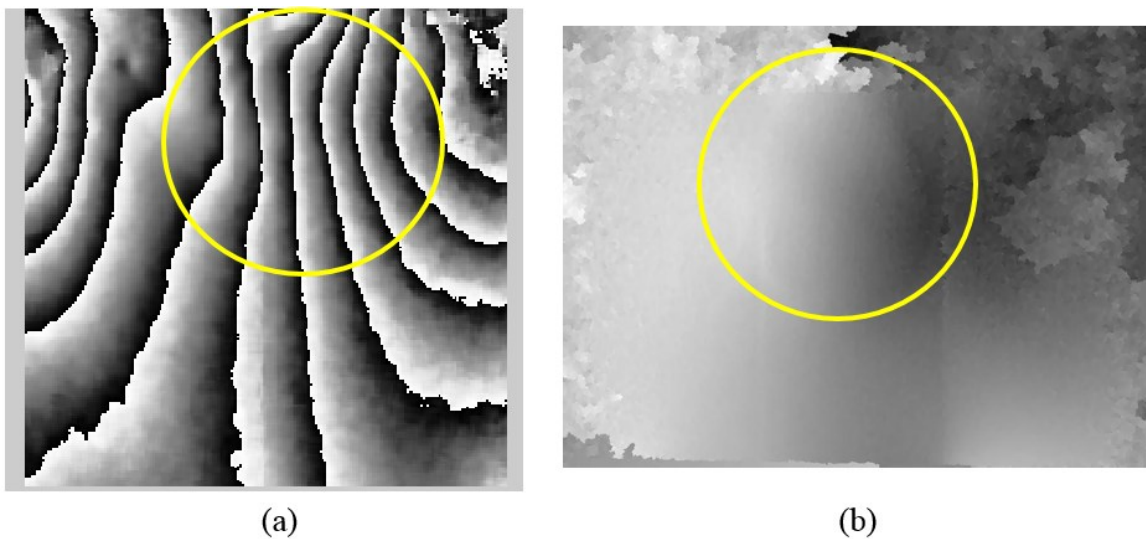
Figure 5.4.   NDT of a composite panel: (a) wrapped phase of deformation gradient along the horizontal direction, and (b) corresponding unwrapped phase.

Because defects in an image can be characterized by high value first derivative, in order to highlight the defects in the phase map, first derivative of the phase map is performed by calculating image derivatives in a horizontal direction

$$\Omega'(x,y) = \frac{\partial \Omega}{\partial x}(x,y), \tag{44}$$

which is the second derivative of the displacement of the panel under thermal loading. Because the measurement induces a 3-second period of thermal loading followed by 5 seconds of cooling time and the camera frame rate is 40Hz, the resulting data set is of 320 images and 80 phase maps. To enhance the shearography results, we calculate each phase derivative in a horizontal direction to a cumulative slope of the horizontal shearography phase map, which is shown in Figure 5.5, thus enabling the identification of structural defects within the panel.
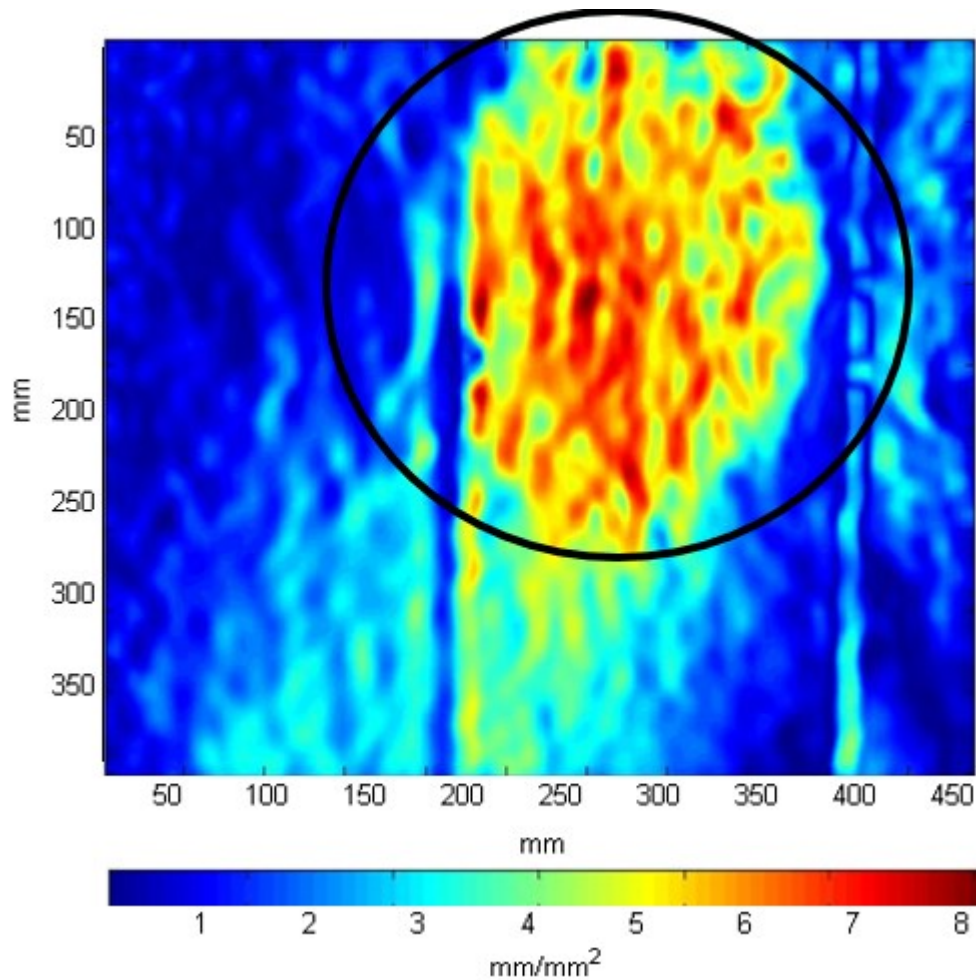
Figure 5.5.   Cumulative results of continuous 8-second recording during a thermal cycle: 3-second thermal loading and 5-second cooling. Noted are areas of large strain slopes, which indicate defects in the sample

Based on the workflow we developed in Chapter 1, in the last step of using laser shearography to perform NDT, a multimedia projector is induced to project the shearography results back on the surface of the real sample.   The transfer function obtained in Chapter 4 can be applied to map the shearography results to the coordinates of projector. After applying the transfer function on the shearography results captured by the

shearography setup shown in Figure 5.6, the newly registered image is projected back onto

the sample's surface, based on the locations of shearography system and projector, in order

to localize the defect on the sample. This aids in the process of marking defects on real

samples to make it easier for engineers to identify the actual location of defects on real

samples [Chen et al., 2014].
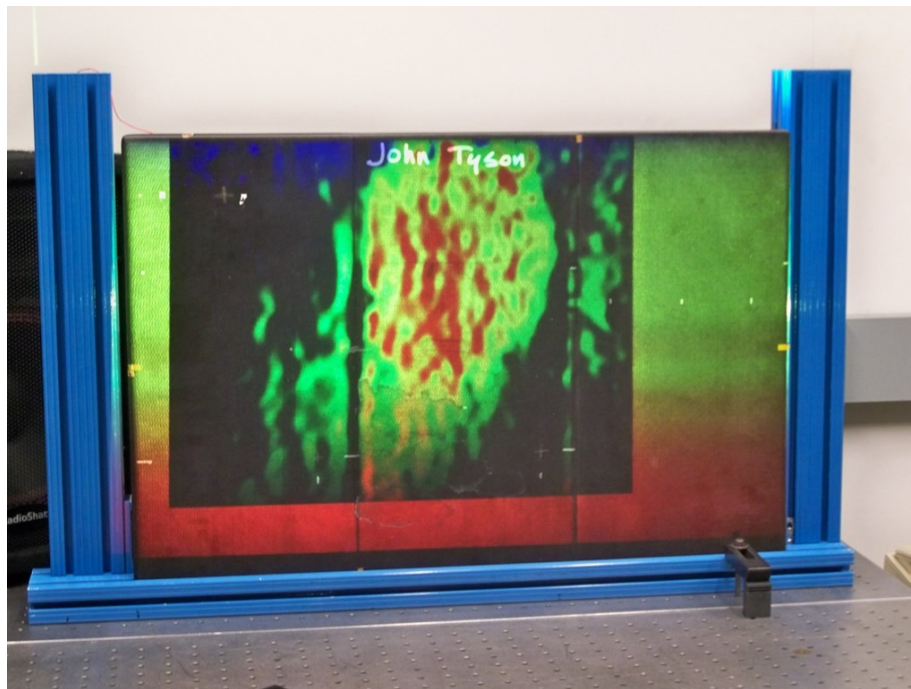
Figure 5.6. Shearography crack location results projected back onto the real sample

5.2 NDT of human TM characterized by laser shearography

In the human body, shearography can also be used as a diagnostic tool. Shearography

has several advantages over other tools—especially its resiliency to environmental

disturbances. One such application is in the characterizing of the tympanic membrane

(TM), which is located in the terrestrial vertebrate middle ear as shown in Figure 5.7.
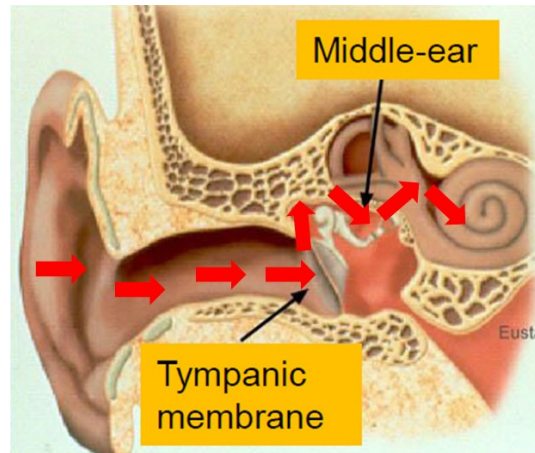
Figure 5.7.   Components of the human ear and sound transmission path
from the outer ear to the inner ear

The TM is responsible for converting sound waves captured by the outer-ear into vibrations in the middle-ear [Rosowski et al., 2009; Cheng et al., 2010; Rosowski et al., 2013, Khaleghi et al., 2013].   Correctly characterizing the TM's function is limited in current diagnostic tools, which are often disturbed by environmental factors such as outer and inner vibrations, including the patient's heartbeat and breathing [Dobrev et al., 2013]. Shearography, however, is not susceptible to such environmental disturbances, and it is able to measure the derivative of displacement directly with lower coherence requirements. This makes shearography an exceptionally low cost and effective method for characterizing the TM. Current, we are developing a Digital Sheaography System (DSS) as a tool for the

quantification of the acoustically induced response of the TM [Rosowski et al., 2009; Cheng

et al., 2010; Rosowski et al., 2013; Khaleghi et al., 2013; Dobrev et al., 2013; Furlong et al.,

2013].   The system is being built for in-vitro testing, as shown in Figure 5.8 and 5.9
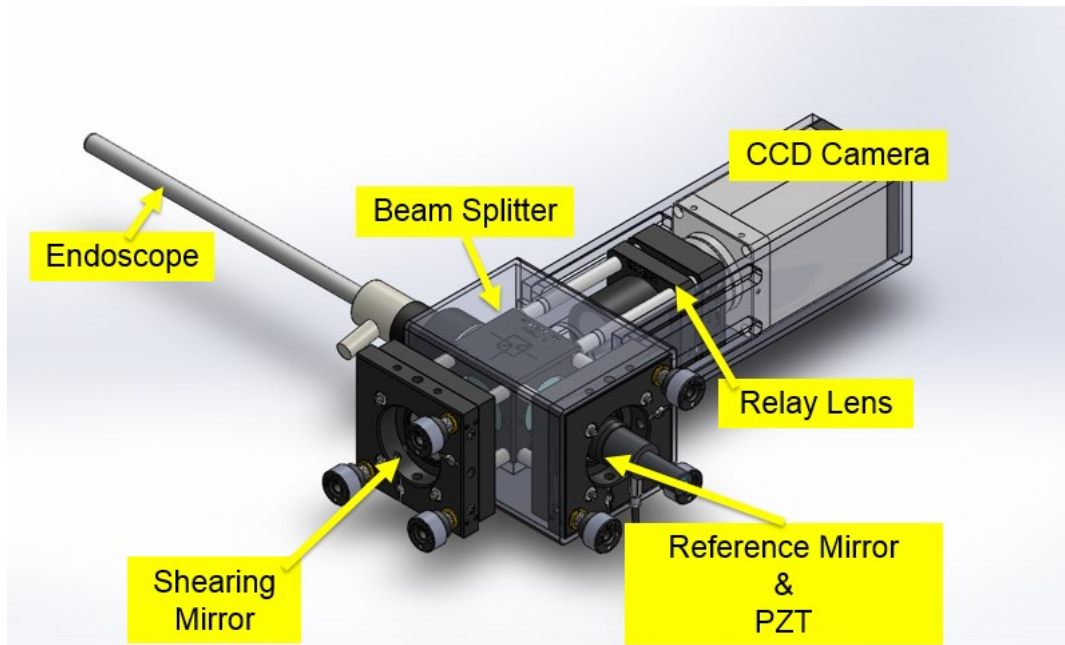
Figure 5.8. CAD model of a Digital Shearography System (DSS) being developed for
quantification of the acoustically induced response of the TM
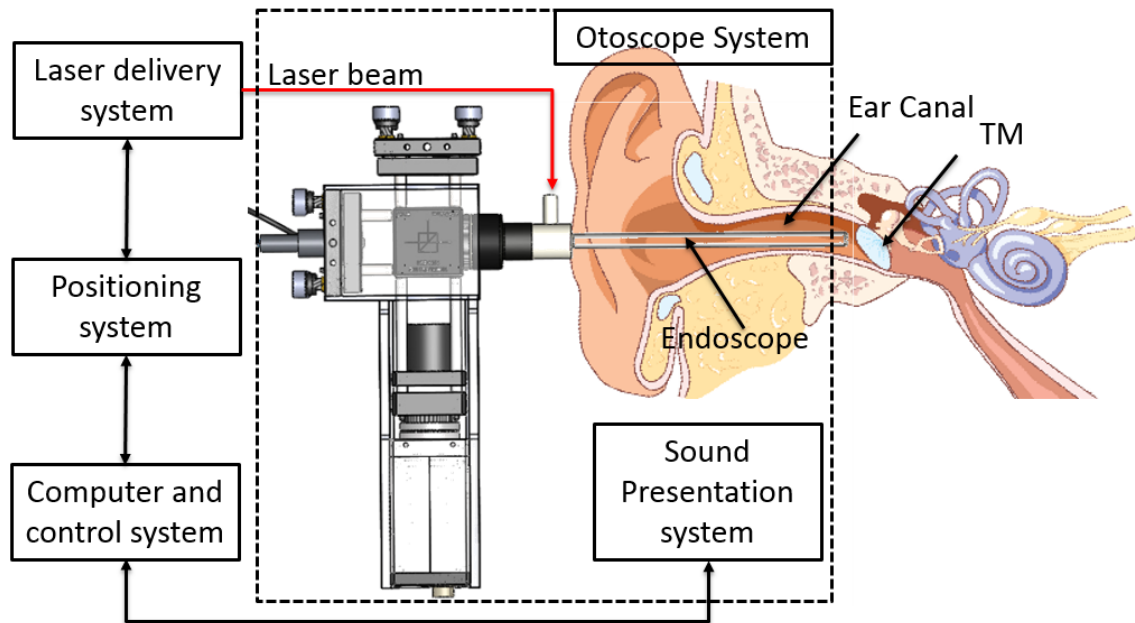
Figure 5.9.   Ideal schematic view of the single-axis Shearography system. The measurement and sound presentation systems are located within the otoscope system

The experiment setup uses an earphone speaker to induce acoustic loading, which is shown in Figure 5.10a.   The full experiment setup is shown in Figure 5.10b.   The first prototype uses objective lens rather than endoscope to prove the concept of DSS.   The optical head was located at a working distance of 0.5m from the membrane.   In this Thesis, we use a latex thin membrane to simulate the TM, as shown in Figure 5.11.   Object illumination for shearography is provided by a pulsed laser with pulse energy of 0.2mJ with a wavelength of 532nm
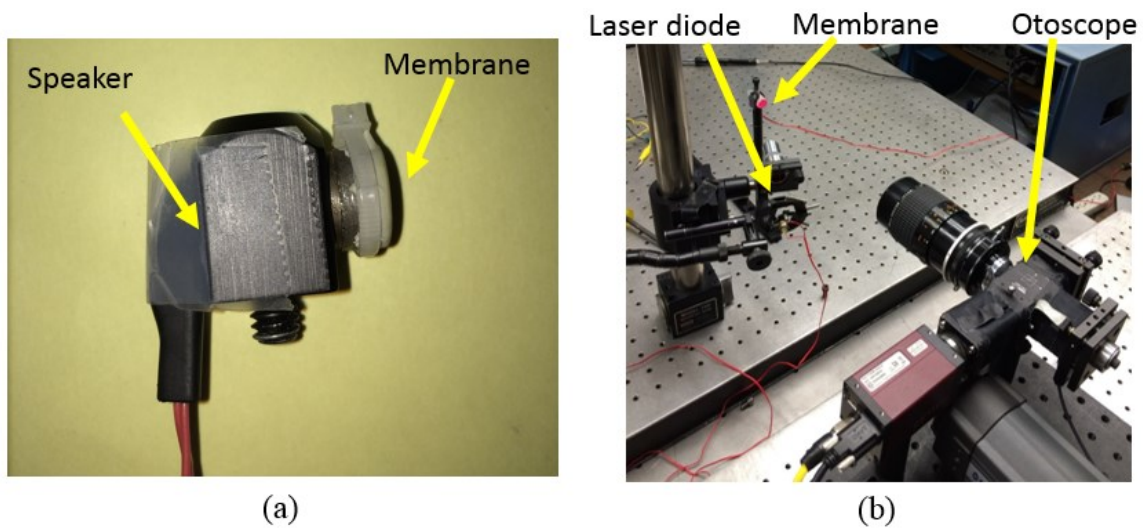
Figure 5.10.   NDT of a thin membrane: (a) the membrane subjected to acoustic excitation by a speaker; (b) the shearography system aimed at a thin membrane under examination.
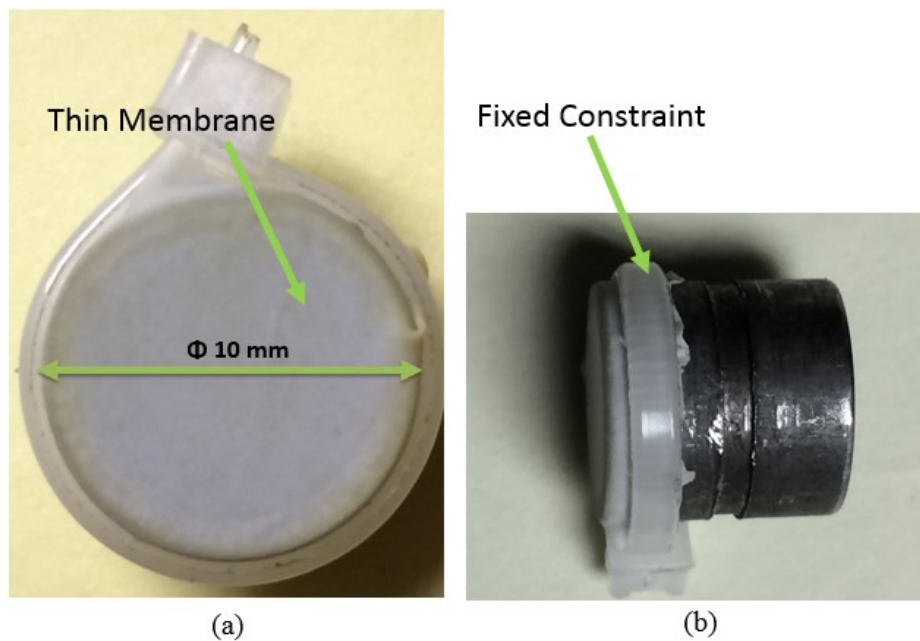
Figure 5.11.   Sample of interest, (a) the diameter of thin membrane is 10mm; (b) the boundary condition is fixed constraint

Before testing the sample, acoustic loading simulation is performed in COMSOL by using eigenvalue analysis, as shown in Figures 5.12 and 5.13. Eight Eigen frequencies are investigated. Corresponding predictions of wrapped phase and modulation fringes are shown in Figures 5.12 and 5.13.
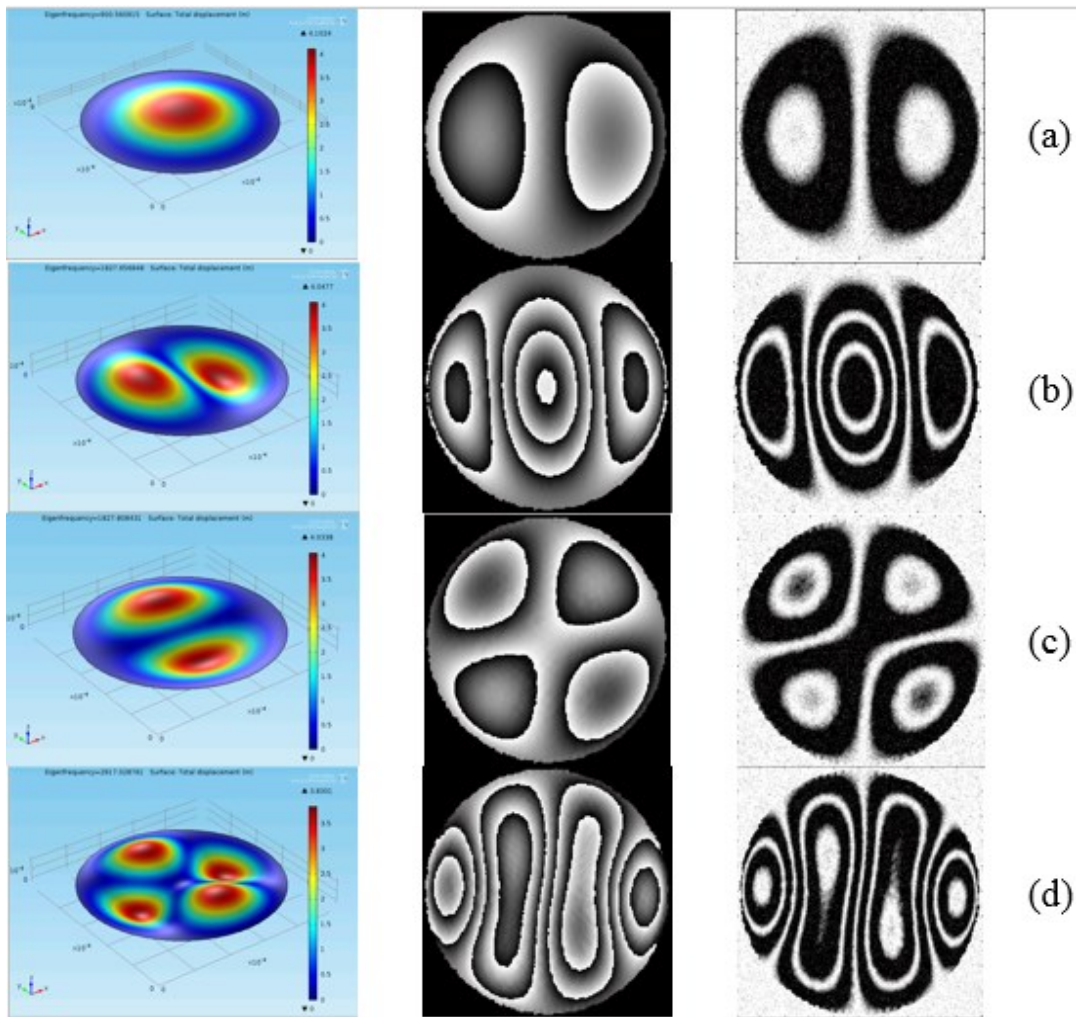
Figure 5.12.   Deformation of a thin membrane corresponding to the first set of four modes of vibrations obtained from FEA analysis, corresponding prediction of shearographic wrapped phase and modulation fringes: (a) 900Hz; (b) 1827.5Hz; (c) 1827.8Hz; (d) 2917Hz, respectively.
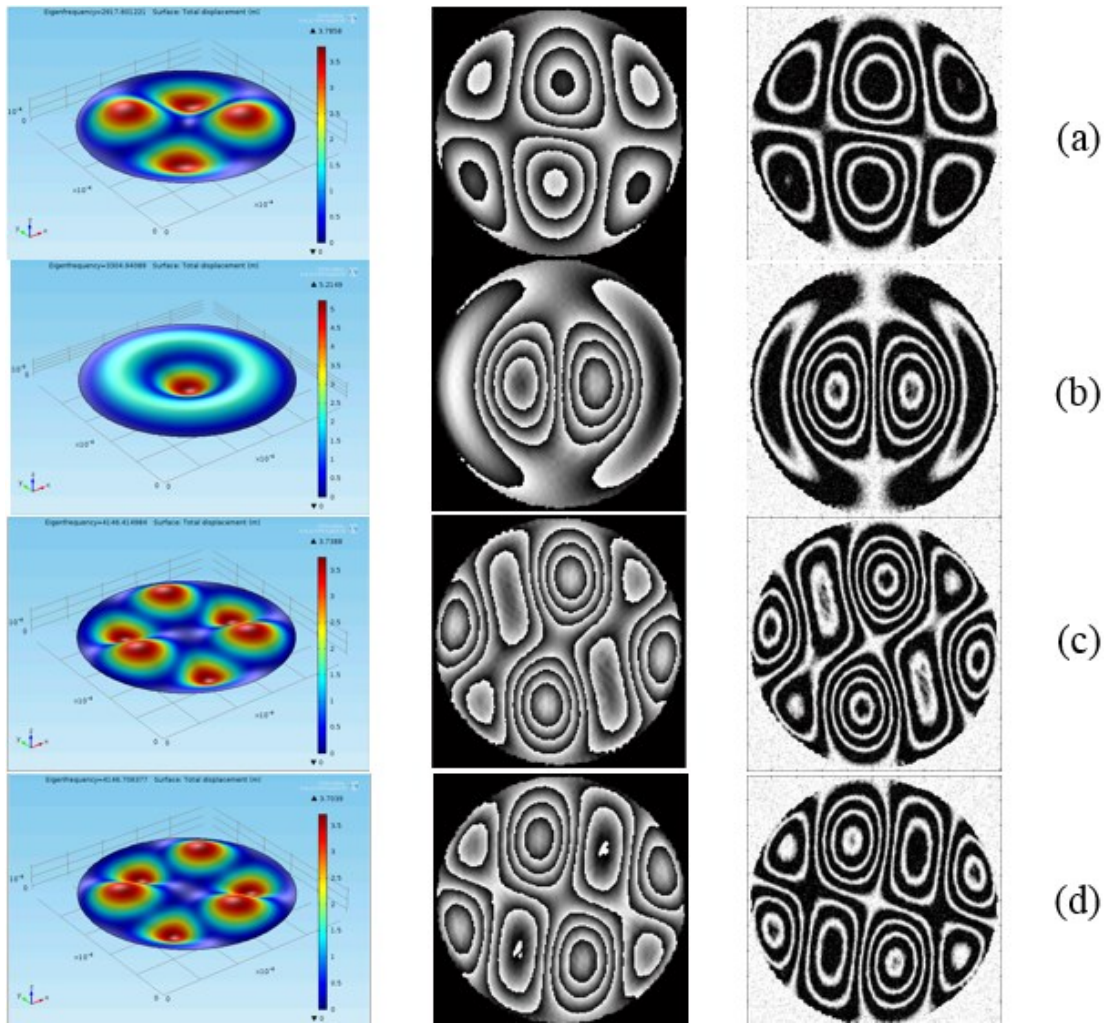
Figure 5.13.   Deformation of a thin membrane corresponding to the second set of four modes of vibrations obtained from FEA analysis, corresponding prediction of shearographic wrapped phase and modulation fringes: (a) 2917.6Hz; (b) 3305Hz; (c) 4146.4Hz; (d) 4146.7Hz, respectively.

Defects are intentionally made in the sample, as shown in Figure 5.14.   There are two types of defects made: the first is circular holes, and the other is a small crack.   All of the defects were made by a heated pin.   The diameter of the two circular holes are in the order of 0.7mm.   The location of the defects is shown in Figure 5.14.
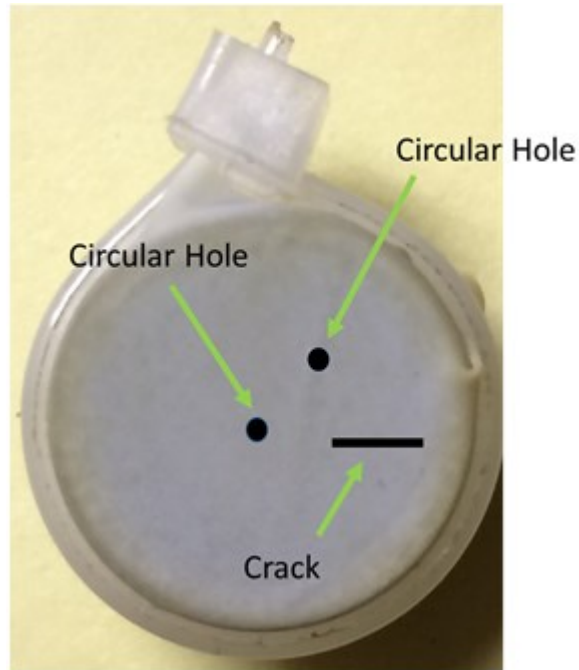
Figure 5.14. A thin membrane with two defects as the sample of interest.

During acoustic loading, to gain quantifiable insight into the precise movements of the object, a stroboscopic method is used. The illumination source, a pulsed laser, is synchronized with the stimulus, as well as the camera acquisition, so that the system is seeing only a desired phase position of the stimulus vibration cycle [Khaleghi et al., 2014]. By analyzing the phase positions throughout the stimulus cycle, we can precisely control the strobe phase position to detect defects more accurately. An overview of the shearography system that uses the stroboscopic measurement technique is shown in Figure 5.15.
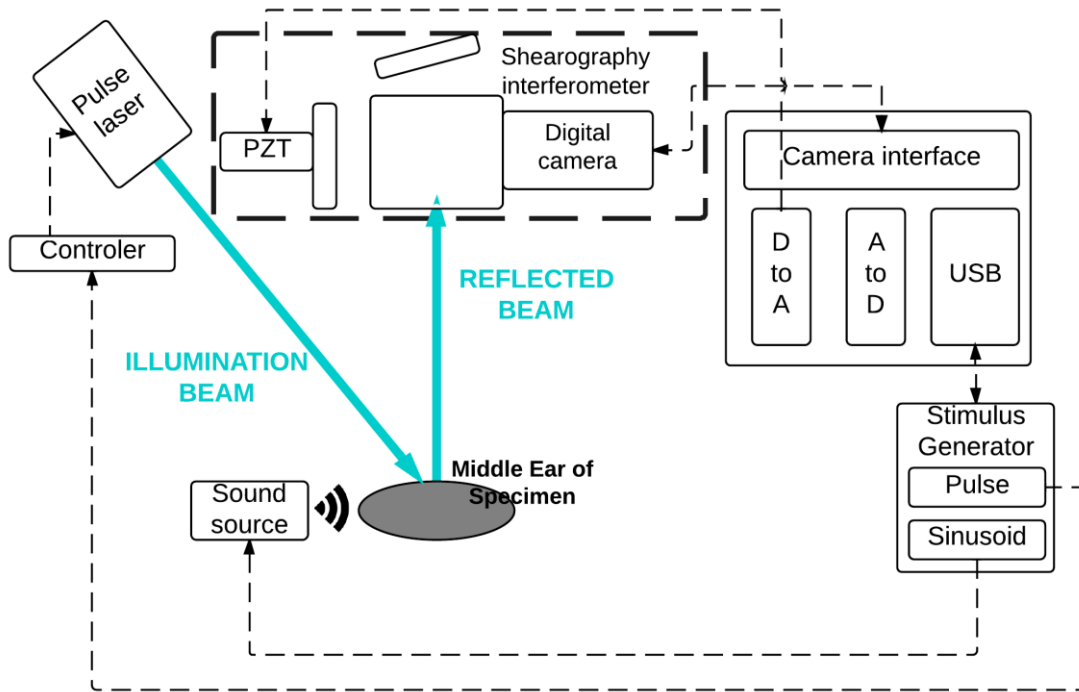
Figure 5.15.   Stroboscopic measurement via computer-assisted shearography

Sound stimuli were continuous tones at eight difference frequencies: 2.45, 3.115, 2.231, 3.115, 3.142, 3.593, 3.446, and 3.601 kHz, with input power at 5v, 1.5 amp so as to produce measurable sound-induced membrane displacements in the shearography images. The voltage waveforms were generated by the computer-controlled stimulus generator (AFG 3102 Tektronix), which also generated the 'strobe' pulses to activate the 'strobe switch.'

At each measurement frequency, we recorded eight shearograms of the membrane evenly spaced in the stimulus phase over one stimulus cycle, as shown in Figure 5.16.   We

also captured one reference shearogram, a preliminary measurement at the zero stimulus phase. The gradient of displacement of the membrane at the eight stimulus phases are thereafter computed relative to the reference displacement [Rosowski et al., 2009; Cheng et al., 2010, Khaleghi et al., 2014].
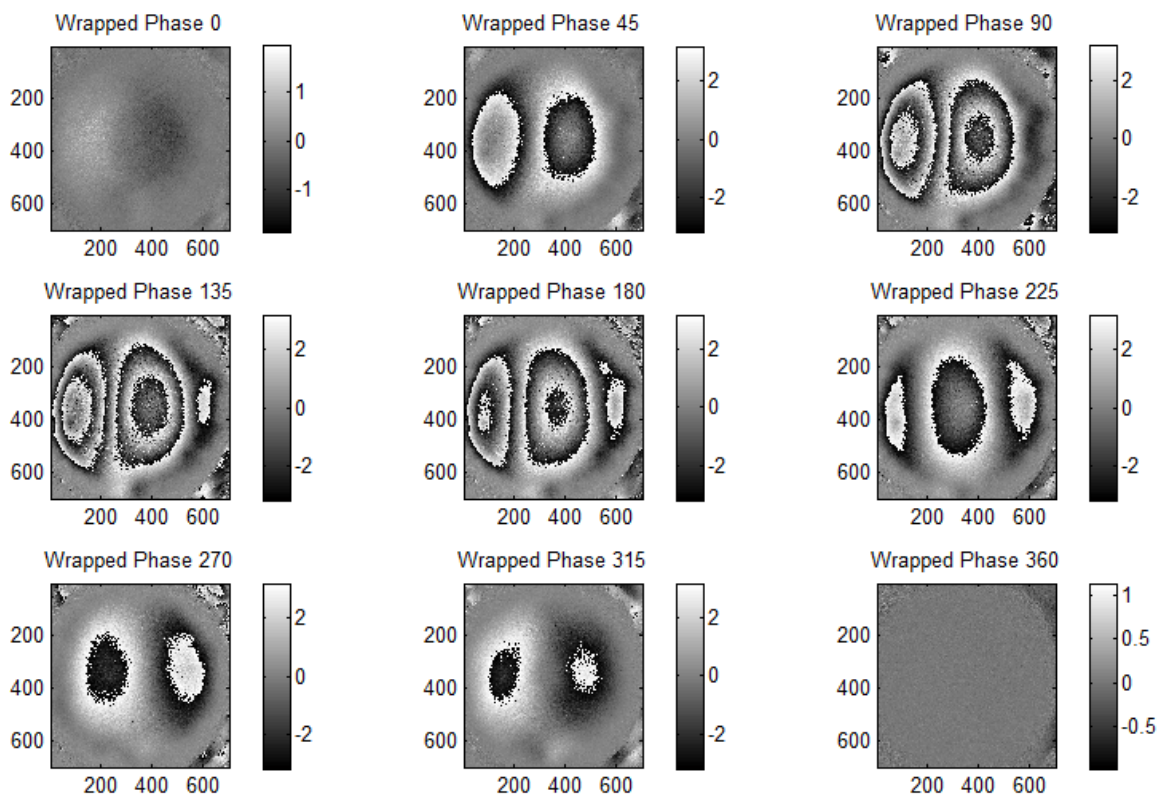
Figure 5.16. Stroboscopic shearograms of the thin membrane recorded at eight stimulus phases (0, $\pi/4, \pi/2...7\pi/4$) at 2.45kHz, in which the motion of the thin membrane is relative to the reference shearogram. Optical wrapped phase varies from -$\pi/2$ to $\pi/2$

Figure 5.17 shows the wrapped phase map at 45 degrees relative to the zero stimulus phase map, and the resulting calculations are performed based on the stroboscopic recording at

3.126KHz.
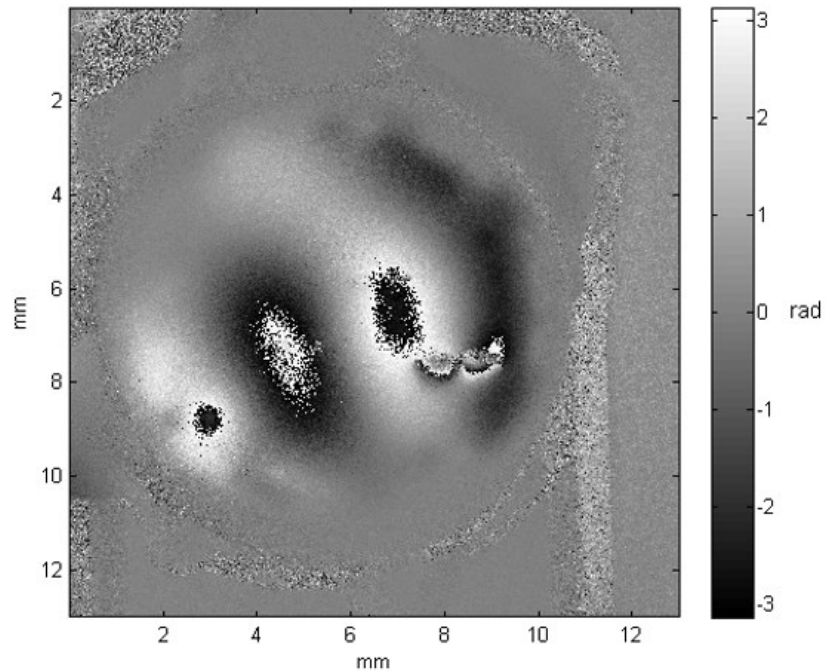
Figure 5.17.   NDT of a thin membrane: wrapped phase of deformation gradient along the horizontal direction. Indicated are areas of irregular wrapped phase fringes indicate defects in the sample

By simply subtracting any stimulus phase from 0 stimulus degree phase, as shown in Figure 5.17, the crack is easily detected.   However, the two circular holes are not as obvious as the crack defect.   In order to highlight the circular hole defects in the phase map, a feature detection algorithm is applied by using a post processing algorithm that calculates the slope of the phase map.   Figure 5.18 shows the feature detection results by calculating the magnitude of the horizontal slope of the phase map and the vertical slope of the phase

map by using

$$|\nabla\Omega|(x,y) = \sqrt{(\frac{\partial\Omega}{\partial x}(x,y))^2 + (\frac{\partial\Omega}{\partial y}(x,y))^2} \qquad (45)$$

Figure 5.18 shows the magnitude of slope of wrapped phase, and Figure 5.18a is the absolute

value of magnitude of the slope of wrapped phase. Figure 5.18b shows the filtered results

of Figure 5.18a, which allows for the identification of structural defects within the sample.
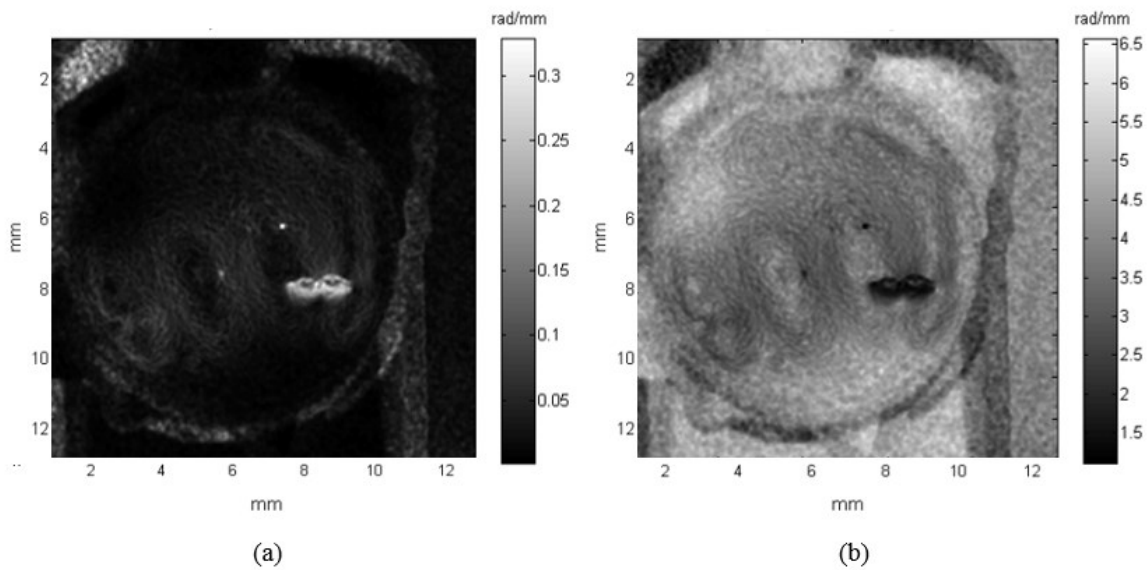
Figure 5.18. NDT of a thin membrane: (a) absolute value of magnitude of the slope of wrapped phase in horizontal and vertical directions; (b) corresponding enhanced results of (a), indicated are areas of irregular sharp color change, which indicate defects in the sample

6. Conclusions and future work

A hybrid approach that combines FEA and fringe prediction is proposed to improve defect detection in structural health monitoring. In our approach, FEA is used to obtain the simulated deformation fields of the objects under different loading conditions, and in turn, corresponding shearographic fringe patterns are predicted. Different types of defects were embedded in FE models, and we then predicted the corresponding shearographic fringes. As an additional step, we projected the shearographic results back onto the actual surfaces of the objects to improve locating and marking the defects on the real sample. The results show that combining FEA, fringe prediction, and fringe re-projection will improve the accuracy and increase the speed of defect detection. Also, one of the limitations of the approach is that if the size of the defects is too small compared with the size of the sample, in that case, finer meshes are needed in order to have convergent FEA-solutions, which leads to a high expensive computation power.

In our future work, we plan to use this hybrid approach to simulate more complex geometry, such as sandwich structures and honeycomb composites. Some of the dangerous flaws in such structures that can be produced by in-service and environmental stresses are delamination and internal cracks, which are critical issues in the aerospace industry due to their impact on safety and performance. Our hope is that the approach of combining FEA, shearography fringe prediction simulation, and inducing a projector to

visualize the location of defects on the sample can be applied in real inspection procedures.

References

K.M.Bajoria, "Non Destructive Testing Of Structures", Seminar, 2009, http://www.epernicus.com/shared_documents/749/seminar.pdf?554da9d585db. Last accessed: May 2014

N. D. Bapat, *Development of sound presentation system (SPS) for characterization of sound induced displacements in tympanic membranes*, M.Sc Thesis, Mechanical Engineering, Worcester Polytechnic Institute, 2011.

K. Creath, "Phase-shifting speckle interferometry", *Applied Optics* 24(18): 3053-3058, 1985

X. Chen, M. Khaleghi, I. Dobrev, W. Tie, C. Furlong, "Structural health monitoring by laser shearography: experimental and numerical investigations," *Proc. SEM* 2014, Annual Conference & Exposition on Experimental and Applied Mechanics, Greenville, SC, 2014

COMSOL Multiphysics, http://www.comsol.com.   Last accessed: May 2014

ANSYS Tutorial Website, Cornell University. https://confluence.cornell.edu/pages/viewpage.action?pageId=127118400.   Last accessed: May 2014

J. Cheng, A. Aarnisalo, E. Harrington, M. Hernandez-Montes, C. Furlong, S. Merchant, J. J. Rosowski, "The motion of the surface of the human tympanic membrane measured with stroboscopic holography," *Hear. Res.,* 263(1): 66-77, 2010

P. M. de Larminat, and R. P. Wei, "Normal surface displacement around a circular hole by reflection holographic interferometry," *Exp. Mech.,* 18(2): 74-80, 1978

I. Dobrev, E. J. Harrington, T. Cheng, C. Furlong, and J. J. Rosowski, "Digital holographic otoscope for measurements of the human tympanic membrane in-vivo," *Proc, SEM,* Imaging Methods for Novel Materials and Challenging Applications, 3:39-45, Springer Verlag, New York, 2013

I. Dobrev, J.M. Flores Moreno, C. Furlong, E. J. Harrington, J. J. Rosowski, and C. Scarpino, "Design of a mechatronic positioner for a holographic otoscope system," *Proc. SEM 2011*, 2, 193-198, 2012

I. Dobrev, J.M. Flores Moreno, C. Furlong, E. J. Harrington, J. J. Rosowski, and C. Scarpino, "Design of a positioning system for a holographic otoscope," *Proc. SPIE 7791*, interferometry XV: Applications, 77910D, 2010

I. Dobrev, C. Furlong, J.T. Cheng, and J. J. Rosowski, "Acousto-mechanical response of the human TM characterized by high-speed digital holographic methods," *Fringe 2013*, 657-660, Springer Berlin Heidelberg, 2014.

I. Dobrev, C. Furlong, J. J. Rosowski, J. T. Cheng, and E. J. Harrington, "Implementation and evaluation of single frame recording techniques for holographic measurements of the tympanic membrane in-vivo," *Proc. SEM 2013*, Annual Conference & Exposition on Experimental and Applied Mechanics, 3, 85-95, 2014

Engineeringtoolbox website, http://www.engineeringtoolbox.com/ndt-non-destructive-testing-d_314.html. Last accessed: May 2014

C. Falldorf, W. Osten, and E. Kolenovic, "Speckle shearography using a multiband light source," *Opt. Lasers Eng.,* 40(5):543-552, 2003

C. Falldorf, S. Osten, C. Kopylow, and W. Jüptner, "Shearing interferometer based on the birefringent properties of a spatial light modulator," *Opt. Letters* 34(18):2727-2729, 2009

A. V. Fantin, D. P. Willemann, and A. Albertazzi, "Improvements in the marking of defects on large structures surfaces during shearographic inspection," *Proc. SPIE Optical Engineering+ Applications*. International Society for Optics and Photonics, 2012

C. Furlong, I. Dobrev, J.J. Rosowski, and J.T. Cheng, "Assessing eardrum deformation by digital holography," *SPIE* newsroom, 2013

C. Furlong, I. Dobrev, E. Harrington, P. Hefti, and M. Khaleghi, "Miniaturization as a key factor to the development and application of advanced metrology systems," *Proc. SPIE Speckle 2012*, 84130T-84130T, 2012

D. Francis, R. P. Tatam, and R. M. Groves, "Shearography technology and applications: a review", *Meas. Sci. Tech.,* 21:1-29, 2010

Z. Ge, F. Kobayashi, S. Matsuda, and M. Takeda, "Coordinate-transform technique for closed-fringe analysis by the Fourier-transform method," *Appl. Opt.*, 40, 1649-1657, 2001

D. C. Ghiglia, and M.D. Pritt, *Two-dimensional phase unwrapping: theory, algorithms, and software*, New York, Wiley, 1998

R. C. Gonzalez, R.E. Woods, and S. L. Eddins, *Digital image processing using MATLAB*, Pearson Education India, 2004

R. M. Groves, E. Chehura, W. Li, S.E. Staines, S.W. James, and R.P. Tatam, "Surface strain measurement: a comparison of speckle shearing interferometry and optical fibre Bragg gratings with resistance foil strain gauges," *Meas. Sci. Technol.* 18(5):1175, 2007

R. T. Haftka, E.P. Scott, and J.R. Cruz, "Optimization and experiments: a survey," *Appl. Mech. Rev.*, 51(7): 435-448, 1998

E. Harrington, I. Dobrev, N. Bapat, J. M. Flores, C. Furlong, J.J. Rosowski, J.T. Cheng, C. Scarpino, and M. Ravicz, "Development of an optoelectronic holographic platform for otolaryngology applications," *Proc. SPIE Optical Engineering+ Applications*, 77910J-77910J, 2010

Y. Y. Hung, "Shearography: a new optical method for strain measurement and nondestructive testing," *Opt. Eng.* 21(3):213391-213391, 1982

Y. Y. Hung, "Shearography for non-destructive evaluation of composite structures," *Opt. Lasers Eng.,* 24(2): 161-182, 1996

Image registering tutorial website, University of Dayton, http://www.johnloomis.org/ece564/notes/tform/image_reg/reg1/image_reg1.html. Last accessed: May 2014

P. R. Joshi, *Pulsed-Laser excited photothermal study of glasses and nanoliter cylindrical sample cell based on thermal lens spectroscopy*, Ph.D. Dissertation, Utah State University, 2010

M. Kalms, and W. Osten, "Mobile shearography system for the inspection of aircraft and automotive components," *Opt. Eng.,* 42(5):1188-1196, 2003

T. Kreis, *Handbook of holographic interferometry: optical and digital methods*, Wiley-VCH, 2005

M. Khaleghi, I. Dobrev, E. Harrington, P. Klausmeyer, M. Cushman, and C. Furlong, "Long-term effects of cyclic environmental conditions on paintings in museum exhibition by laser shearography," *Advancement of Optical Methods in Experimental Mechanics*, 3: 283-288, 2014

M. Khaleghi, I. Dobrev, E. Harrington, C. Furlong, and J. J. Rosowski, "Study of the transient response of Tympanic Membranes under acoustic excitation," *SEM 2013*, In Mechanics of Biological Systems and Materials, 4: 1-9, 2014

M. Khaleghi, I. Dobrev, P. Klausmeyer, E. Harrington, and C. Furlong, "Investigation of thermomechanical effects of lighting conditions on canvas paintings by laser shearography," *Proc. SPIE 8494*, Interferometry XVI: Applications, 84940A; DOI:10.1117/12.958089, 2012

M. Khaleghi, C. Furlong, J. T. Cheng, and J. J. Rosowski, "3-Dimensional quantification of surface shape and acoustically-induced vibrations of TM by digital holography," *Fringe 2013*, 599-602, 2014

M. Khaleghi, W. Lu, I. Dobrev, J. T. Cheng, C. Furlong, J. J. Rosowski, "Digital holographic measurements of shape and three-dimensional sound-induced displacements of tympanic membrane," *Opt. Eng.*, 52(10), 101916-101916, 2013

The mathworks, www.mathworks.com.   Last accessed: 2014

A. Maceri, *Theory of elasticity,* Springer, 2010

S. Nagpal, N. Jain, and S. Sanyal, "Stress concentration and its mitigation techniques in flat plate with singularities-a critical review," *Engineering Journal* 16(1): 1-16, 2011

W. Osten, E. Garbusi, D. Fleischle, W. Lyda, C. Pruss, R. Reichle, and C. Falldorf, "Optical metrology: from the laboratory to the real world," *Proc. SPIE Speckle 2010*, 73871G-73871G, 2010

W. Osten, W. P. O. Jüptner, and U. Mieth, "Knowledge-assisted evaluation of fringe patterns for automatic fault detection," *Proc. SPIE International Symposium on Optics, Imaging, and Instrumentation*, 256-268, 1993

R. Prakash, *Non-Destructive Testing Techniques*, New Academic Science, 2009

R. J. Pryputniewicz, "Electronic shearography and electronic holography working side by side," *Proc. SPIE* 1821 Industrial Applications of Optical Inspection, Metrology, and Sensing, 27, 1993

R. J. Pryputniewicz, "Hybrid approach to deformation analysis," *Proc. SPIE* 2342, Interferometry '94: Photomechanics, 282-296, 1994

J.J. Rosowski, J.T. Cheng, M.E. Ravicz, N. Hulli, Mds. Hernandez-Montes, E. Harrington, C. Furlong, "Computer-assisted time-averaged holograms of the motion of the surface of the mammalian tympanic membrane with sound stimuli of 0.4 to 25 kHz," *Hear. Res.,* 253(1):83–96, 2009

J. J. Rosowski, I. Dobrev, M. Khaleghi, W. Lu, J. T. Cheng, E. Harrington, and C. Furlong, "Measurements of three-dimensional shape and sound-induced motion of the chinchilla tympanic membrane," *Hear. Res.,* 301, 44-52, 2013

M. Takeda, H. Ina, and S. Kobayashi, "Fourier-transform method of fringe-pattern analysis for computer-based topography and interferometry," *J. Opt. Soc. Am*., **72**:156-160, 1982

E. Tripp, *Interferometric optical readout system for a MEMS infrared imaging detector*, M.Sc Thesis, Mechanical Engineering, Worcester Polytechnic Institute, 2012

M.J. Zervas, *Development of a high speed, robust system for full field-of-view 3D shape measurements*, M.Sc Thesis, Mechanical Engineering, Worcester Polytechnic Institute, 2011

Appendix A: Matlab program for shearography fringe prediction

```matlab
clear all
close all
clc

%% Read excel data

asa7 = xlsread('D:\New folder\Thesis\Comsol_file\pmma_sound_467.xlsx');

TF = isnan(asa7);


[xi,yi] = meshgrid(0:0.0005:0.2032,0:0.0005:0.09525);
X_disp = griddata(asa7(:,1),asa7(:,2),asa7(:,4),xi,yi,'cubic');
Y_disp = griddata(asa7(:,1),asa7(:,2),asa7(:,5),xi,yi,'cubic');
Z_disp = griddata(asa7(:,1),asa7(:,2),asa7(:,6),xi,yi,'cubic');

[X_FX,X_FY] = gradient(X_disp,0.0005,0.0005);
[Y_FX,Y_FY] = gradient(Y_disp,0.0005,0.0005);
[Z_FX,Z_FY] = gradient(Z_disp,0.0005,0.0005);




wavelength = 533*10e-6;
shear_amont = 15; % 1- 10 mm
system_parameter=pi*shear_amont/wavelength;

camera = [0 0 1];
laser = [0 0 1];

h= 0;
[rows cols]=size(X_FX);
for i    = 1:rows
     for j = 1:cols
```

```matlab
            h = h+1;
            index(h,:,:,:,:,:,:,:) = [xi(i,j) yi(i,j) 0 X_FX(i,j) Y_FX(i,j) Z_FX(i,j)];
        end
end
camera = [0 0 10];
laser = [0 0 10];
for i = 1: length(index(:,1))

    b(i,:,:,:) = (camera - [index(i,1) index(i,2) index(i,3)])/(norm(camera-[index(i,1)
index(i,2) index(i,3)]));
    s(i,:,:,:) = ([index(i,1) index(i,2) index(i,3)] - laser)/(norm(([index(i,1) index(i,2)
index(i,3)] - laser)));
end
e = (b - s);




for i = 1: length(index(:,1))
unwrap_im(i,:) =
system_parameter.*(e(i,1).*index(i,4)+e(i,2).*index(i,5)+e(i,3).*index(i,6));
end

index1 = [index(:,1) index(:,2) index(:,3) unwrap_im(:,1)];
vi = griddata(index1(:,1),index1(:,2),0.00003.*index1(:,4),xi,yi,'linear');


im = mod(vi + pi, 2*pi) - pi;
    figure;imagesc(im);colormap gray
    axis image
        imwrite(im,'712uwrap.bmp')
Iim = cos(im);
figure;imagesc(Iim);colormap gray
axis image

  imwrite(Iim,'712.bmp')
    J = imnoise(Iim,'gaussian');
```

Appendix B: Matlab program for shearography results re-projection

```matlab
close all;
clear;
clc;


base = zeros(800, 1280);
base (400:600, 600:800) =1;
imagesc(base);axis image



image_dir =('D:\Share_drive\Thesis\Comsol&matlab\predict_fringe\aaa');

Target_im_name1 = 'base_v2.jpg';
Target_im_name2 = 'input.tif';



input = imread(strcat(image_dir, '\', Target_im_name2));



base = double(base);
input = double(input(:,:,1));
input_new = mat2gray(input);
input_new = im2bw(input_new,0.11);
    figure;imagesc(input_new);axis image
    figure;
    imagesc(base);axis image

base_points = [11 11; 41 71];
input_points = [14 44; 70 81];
[aerial_points,ortho_points] =
cpselect(input_new,base,input_points,base_points,'Wait',true);


input_points_adj = cpcorr(aerial_points,ortho_points,input,base);
```

```matlab
t_concord = cp2tform(input_points_adj,ortho_points,'projective');
info = imfinfo('base_plate_4.jpg');


input_registered = imtransform(input_new, t_concord,...
                                    'XData',[1 info.Width],...
                                    'YData',[1 info.Height]);




figure
subplot(1,2,1)
imshow(input_new); title('Input Image')
axis image
axis on

subplot(1,2,2)
imshow(input_registered);    title('input registered')
axis image
axis on
hold on
imwrite(input_registered,'input_registered.jpg')


image_dir =('D:\Share_drive\Thesis\Comsol&matlab\predict_fringe\aaa');
Target_im_name1 = 'results_run20001.tiff';

test = imread(strcat(image_dir, '\', Target_im_name1));
test = double(test(:,:,1));


test_registered = imtransform(test, t_concord,...
                                    'XData',[1 info.Width],...
                                    'YData',[1 info.Height]);
figure
subplot(1,2,1)
imagesc(test)
axis image
```

```matlab
axis on

subplot(1,2,2)
imagesc(test_registered)
colormap gray
axis image
axis on

test_registered_nomalized = mat2gray(test_registered);

imwrite(test_registered_nomalized,'test_registered_nomalized.tif','compression' ,'none')




test_registered_saved = imread('test_registered_nomalized.tif');

figure;imagesc(test_registered_saved)
colormap gray
axis image
axis on

%% enhance the results
[g ,t] = edge(test_registered, 'log',50,0.4);

figure;imagesc(g)
colormap gray
axis image
axis on
```

Appendix C: Matlab image processing program for branching process

NDT of thin membranes by laser shearography

```matlab
clear all
close all
clc


%% read data-rti

directory = 'D:\Research\Shearography\shearogaphy_memb\DATA5';
file_name_base = '3.126Khz_test';

[I_all,frameH, frameW,IvvMetadata1,rtiMetadata] = read_RTI_4_steps_DE(directory,
file_name_base);

%% read lvvd


filePath =
'D:\Research\Shearography\shearogaphy_memb\DATA5\3.126Khz_ampl_1.5_Feb_17_bi
g_LINE_X.lvvid';
%file_name_base = '3.126Khz_test';
% def_frame =1;
% ref_offset = 5;
% ref_frame = def_frame   - ref_offset;
% ref_frame = 34;

def_frame = 52;
ref_offset = 5;
ref_frame = def_frame    - ref_offset;
%ref_frame = 52;

steps    = 4;
```

```matlab
[I_ref,frameH, frameW,IvvMetadata1,rtiMetadata] =
extractLvvidFrame(filePath,ref_frame,steps);
[I_def,frameH, frameW,IvvMetadata1,rtiMetadata] =
extractLvvidFrame(filePath,def_frame,steps);

I_all = cat(3,I_ref,I_def);
%[I_all,frameH, frameW,IvvMetadata1,rtiMetadata] = read_RTI_4_steps_DE(directory,
file_name_base);



%%% calc phase
dh_param(1)=0;
dh_param(2)=0;
dh_param(3)=0;

espi_param(1)=0;
espi_param(2)=0;
espi_param(3)=0;
holo_method = 0 ;

filt = 1;
filt_type = 1;

[Imod,ImodD,ImodDE,OpPhase,Icomplex] = Holo_calc(I_all,dh_param,espi_param,...
    holo_method,filt,filt_type);



figure;
imagesc(OpPhase)
colormap gray
axis image

%%% gradient - Ellery phase only


filt_size_lowpass = 3;
filt_type =1;
```

```matlab
I4_C_crop_filt = holo_filter_complex(Icomplex,filt_size_lowpass,filt_type);
shiftx =1;
shifty =1;

phase = angle(I4_C_crop_filt);

phase_offx = circshift(phase, [0 shiftx]);
phase_offy = circshift(phase, [shifty 0]);


filt_size = [5 5];

tic
phase_delta_filt = complex(medfilt2(phase_offx - phase, filt_size), medfilt2(phase_offy - phase, filt_size));
toc


figure
imagesc(abs(log(holo_filter(abs(phase_delta_filt),1,2))));
%imagesc(((holo_filter(abs(phase_delta_filt),1,2))));
title(' phase delta filt log abs ')
colorbar
colormap gray
axis image

%%
I1 = mat2gray(abs(phase_delta_filt));
level = 0.5;
I1 = im2bw(I1,level);
I2 = mat2gray(OpPhase);
mix = 0.6;

figure
imagesc(I2.*(1-mix + mix*I1));
title(' phase delta filt ')
colorbar
colormap gray
```

Appendix D: Laser shearography system operating workflow

- Turn System On

- System Setup
  - Laser setting
  - Illumination setting
  - Camera optics setting
  - Adjust the direction and amount shear using FFT in Laserview
  - Calibrate PZT
    - Adjust on offset
    - Run Hariharan experimental algorithm

- Acqustion and processing

  Measurement and processing
  Acoustic analysis
  - Frequency response
    - Switch to time average
    - Adjust exposure time
    - Adjust camera fps if needed.
    - Frequency x to y with steps of z

    Or
    - Frequency x to y using sweep function.
  - Run experiment.
  - Stroboscopic measurements
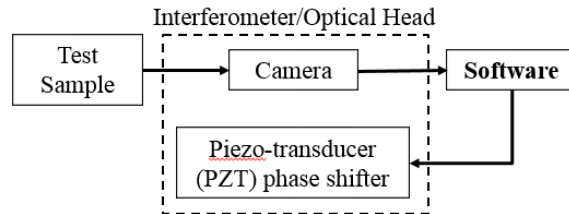 - Analyze for magnitude and phase of response

  Thermal analysis
  - Start recording in time-average mode
  - Excite the sample
  - Stop recording
  - Post-process phase date

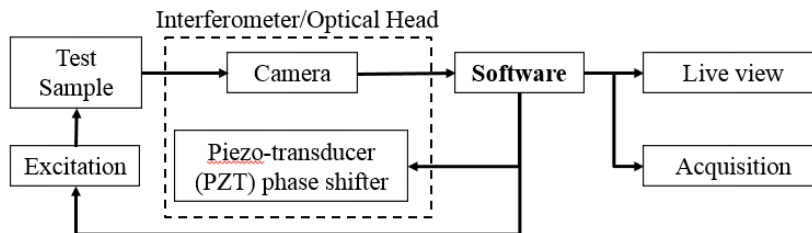- Turn System Off

Appendix E: Shearography system schematic diagram

1. Hardware set up and software controls

- Set up sample
- Set up illumination
- Set up camera and optics – use live view from the software
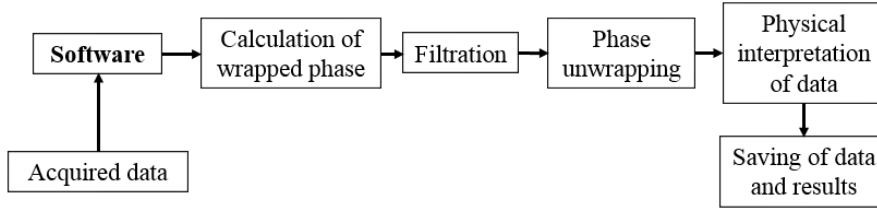- Adjust the shear amount and direction - use FFT in laser view
- Calibrate the PZT

2. Acquisition of Data

Acquisition modes:

- Time-averaged (TA) mode
- Double-exposure (DE) mode

3. Analysis and interpretation of data

- Computation of wrapped optical phase
- Application of filters
- Unwrapping of phase data
- Interpretation of the optical phase to the physical parameter of interest
- Saving of data and results

Software workflow

Setup
- *Laser* - Control of laser power.
- *Camera* – Frame capture, triggering, control of exposure and frame rate control.
- *PZT phase shifter* – calibration and operation.

Acquisition
- *TA acquisition mode*– using dynamic analysis of to identify frequency of oscillation.
- *DE acquisition mode* – used for quantification of the response of the test sample due to controlled excitation.

Analysis and interpretation of data
- *Wrapped optical phase* computation
- *Filtration*
- *Unwrapping* of phase data
- *Interpretation* of the optical phase to the physical phenomenon of interest